R. & M. No. 2693
(11,560, 12,144, 13,090)
A.R.C. Technical Report



MINISTRY OF SUPPLY

AERONAUTICAL RESEARCH COUNCIL
REPORTS AND MEMORANDA

# Some Investigations on Thin Nose-Suction Aerofoils, Parts I and II

*By*

J. WILLIAMS, M.Sc., Ph.D.

Part I

A Comparison of the Stalling Properties of some Thin Nose-Suction Aerofoils

Part II

A Theoretical Investigation on Thin High-lift Aerofoils Specially Designed for Nose-Slot Suction



LONDON: HER MAJESTY'S STATIONERY OFFICE
1952
PRICE 7*s* 6*d* NET

# Some Investigations on Thin Nose-Suction Aerofoils, Parts I and II

*By*

J. Williams, M.Sc., Ph.D.



*Reports and Memoranda No.* 2693

*April*, 1950

*Summary*.—The stalling properties of some thin nose-suction aerofoils already tested have been examined, and further theoretical investigations have been carried out on thin aerofoils specially designed to give high lift with nose-slot suction.

In Part I, the experimental results from stalling tests on thin nose-suction aerofoils are compared and the design features of the tested aerofoils are analysed. The aerofoils include the 8 per cent thick Lighthill and Glauert sections specially designed for nose-slot suction, the 8 per cent thick H.S.A. V section with distributed suction through a porous nose, and some conventional sections of moderate thickness tested in Germany with slot suction at various positions on the nose. The Lighthill and Glauert aerofoils proved quite good without suction, but the increments in $C_{L\,\max}$ due to suction were rather disappointing. The H.S.A. V aerofoil with distributed suction promises to be more economical as regards suction quantities for delaying the stall at full-scale Reynolds numbers, but this needs further confirmation.

Part II describes a theoretical exploration of possible thin nose-slot aerofoils specially designed to have an abrupt fall in velocity where suction is to be applied on the upper surface of the nose. In an attempt to obtain better sections as regards a late stall at practical suction quantities, various symmetrical and cambered shapes were designed by a simple approximate method and the effect of sink action was also estimated. Low-speed stalling tests are to be made on one of the new cambered sections (D.2/4) in order to determine whether the considerable improvements expected are in fact achieved. The effect of the unusual nose shape on the high-speed performance of the section will also need to be examined.

The theoretical formulæ required for the calculation of the velocity distribution and lift of an aerofoil with a sink on its surface, and some detailed notes on the design of the Glauert nose-slot aerofoil, are given in the Appendices.

## PART I

## A Comparison of the Stalling Properties of some Thin Nose-Suction Aerofoils

1. *Introduction*.—Suction at the nose of a thin aerofoil may be employed to delay the stall to a higher incidence and increase the maximum lift. Three thin nose-suction aerofoils have been tested in a 4-ft (National Physical Laboratory) wind tunnel at low airspeeds[1, 2, 3], the Lighthill and Glauert aerofoils with slot suction, and the H.S.A. V aerofoil with distributed suction through a porous nose. The shapes of these aerofoils are shown in Fig. 1, and the results from the stalling tests are compared in Fig. 2. Some conventional aerofoils of moderate thickness, with slot suction at various positions on the nose, have been tested in Germany at low airspeeds[4]. In view of the German results (*see* Table 1), a theoretical examination has been carried out here of the effect of a sink located on the nose of a thin aerofoil (H.S.A. V) with a large nose radius.

$C_{L\,\max}$ and $\alpha_{\max}$ denote the values of the lift coefficient $C_L$ and the incidence $\alpha$ at which $C_L$ first ceases to increase with $\alpha$; the incidence is measured from the zero-lift attitude (without suction), except in the case of the German results. In the diagrams and tables, the velocity $q$ on the aerofoil is given as a fraction of the velocity of the undisturbed stream, and the chordwise distance $x$ from the leading edge as a fraction of the chord. The curves given in the present report for the thin nose-suction aerofoils tested in the 4-ft wind tunnel are not corrected for wind-tunnel interference; the correction to $C_{L\,max}$ is believed to be small.

2. *The Lighthill and Glauert Slot-Suction Aerofoils.*—The shapes of the Lighthill and the Glauert slot-suction aerofoils were calculated by an exact method[5]*. At an upper design incidence, they were designed to have on the upper surface a large steep fall in velocity at the nose, followed by a low steady adverse gradient back to the trailing edge. To prevent separation at the steep velocity fall, the boundary layer is removed through a narrow slot; the adverse velocity gradient aft of the slot is assumed to be insufficient at the upper design incidence to cause separation of the boundary layer behind the slot. The suction quantity required to prevent stalling at and below the design incidence, therefore, should be small. The stall can be delayed to higher incidences by sink action at the slot sufficient to prevent an increase in the adverse gradient aft of the slot, but the suction quantities required are large. The steep velocity fall chosen for the Lighthill aerofoil was a discontinuous drop at the leading edge, from an infinite to a low velocity, and consequently the aerofoil has a sharp beaked nose. The effect of a narrow slot at the leading edge was not allowed for in the calculations. The Glauert aerofoil has a thin rounded nose with a narrow slot on its upper surface. To enable the slot to be included automatically in the aerofoil shape, the theoretical velocity distribution was assigned for a chosen sink strength.

*Experimental and Theoretical Results.*—Fig. 2 gives measured values of $C_{L\,max}$ and $\alpha_{max}$ plotted against $C_Q$, and Fig. 3 shows some typical lift *vs.* incidence curves at various $C_Q$ values. The $C_{L\,max}$ for both aerofoils without suction is about $1 \cdot 12$, and with suction $C_{L\,max}$ increases to about $1 \cdot 6$ for $C_Q = 0 \cdot 012$. The values of $\alpha_{max}$ without suction are about $13\frac{1}{2}$ deg and $12\frac{1}{2}$ deg for the Lighthill and Glauert respectively; with suction, these values each increase by about 4 deg for $C_Q = 0 \cdot 012$. Unfortunately, the results from the stalling tests are insufficient for a direct comparison of the two aerofoils at other $C_Q$ values. It seems probable that, for a low value of $C_Q$ (boundary-layer suction only), the $C_{L\,max}$ of the Glauert aerofoil would be the higher in view of the improved nose shape. With $C_Q > 0 \cdot 012$, when sink action predominates, the values of $C_{L\,max}$ for the two aerofoils should not differ markedly, as the adverse velocity gradients over the aerofoil upper surfaces at a high incidence are very similar (*see* Fig. 4). The theoretical velocity distribution over the upper surface of the Lighthill aerofoil at a high incidence is shown in Fig. 5 for various sink strengths at the leading edge. It is seen that large sink strengths are necessary to reduce appreciably the adverse velocity gradients.

Fig. 3 shows that the stall is in all cases reasonably gentle. The slope of the experimental lift curves at *low* incidence, when reduced by the factor of 6 per cent to allow for wind-tunnel interference, is about $5 \cdot 7$ per radian for both aerofoils, about 14 per cent lower than the theoretical value of $6 \cdot 6$. It is noticeable that at high incidences below the stall the lift slope is lower for the Lighthill aerofoil than for the Glauert. The flow over the Lighthill aerofoil at incidences just below the stall was investigated by experiments with surface streamers; these tests were not reported in R. & M. 2355[1]. Without suction, the flow separated at the slot but became reattached further along the upper surface, and the position of reattachment moved rearwards as the incidence was increased. With $C_Q \geqslant 0 \cdot 010$, separation occurred first at the rear of the upper surface and the separation point moved forward as the incidence was increased; no reattachment was evident.

The theoretical values of $M_{crit}$ for the Lighthill and Glauert aerofoils without suction are respectively $0 \cdot 73$ and $0 \cdot 72$ at zero lift, and $0 \cdot 68$, $0 \cdot 70$ respectively, at 2 deg incidence from zero-lift†. The velocity gradients over the aerofoils at low incidences remain favourable for only a short distance from the leading edge (*see* Fig. 6).

* The design of the Glauert slot-suction aerofoil has not previously been reported in detail, and is given in Appendix II of the present report.

† Deduced by means of the Kármán compressibility correction for results from incompressible flow; large theoretical velocities in the immediate neighbourhood of the slot are disregarded.

The theoretical and experimental velocity distributions without suction are compared in Fig. 7 for the Lighthill aerofoil and in Fig. 8 for the Glauert aerofoil.

3. *The* H.S.A. V *Aerofoil with Distributed Suction.*—Thwaites designed the H.S.A. V aerofoil by the approximate method[6]. The velocity distribution at low incidence (*see* Fig. 6) was chosen from novel low-drag considerations which have not yet been tested experimentally. The aerofoil has an extremely large nose radius, $0 \cdot 03c$ and consequently the adverse velocity gradients over the nose at high incidence are much less severe than for a normal thin aerofoil. The boundary layer is kept thin and separation from the upper surface prevented, at high incidences, by distributed suction through a porous area (Porosint) over the nose. In early tests the porous area extended to $0 \cdot 15c$ from the leading edge on both the upper and lower surfaces, but later the area was reduced to a half.

*Experimental and Theoretical Results.*—According to approximate theoretical arguments, the value of $C_Q$ required to provide a given increment in $C_L$ at a constant incidence varies with the Reynolds number as $R^{-1/2}$. This was roughly confirmed by the model tests, but experimental verification over a wider range of Reynolds numbers is needed before the results of the model tests can be safely extrapolated to full-scale Reynolds numbers.

Fig. 2 gives the largest values of $C_L$ measured for $\alpha \leqslant 15$ deg, plotted against $C_Q$; $C_{L\,\max}$ and $\alpha_{\max}$ are available only for low values of $C_Q$. Without suction, $C_{L\,\max} = 0 \cdot 87$ and $\alpha_{\max} = 10$ deg when $R = 0 \cdot 58 \times 10^6$. With suction through the full Porosint area and $C_Q = 0 \cdot 0019$, $C_{L\,\max} = 1 \cdot 10$ and $\alpha_{\max} = 14\frac{1}{2}$ deg at the same $R$. When $C_Q = 0 \cdot 0047$, $R = 0 \cdot 24 \times 10^6$, and $\alpha = 15$ deg, $C_L = 1 \cdot 20$ for suction through the full Porosint area and $C_L = 1 \cdot 39$ for suction through the reduced Porosint area; in both cases $C_L$ was still increasing with incidence. An approximate calculation of the corresponding results at $\alpha = 15$ deg and $R = 0 \cdot 58 \times 10^6$ gives $C_L = 1 \cdot 14$ and $1 \cdot 33$ for $C_Q = 0 \cdot 003\,[\equiv 0 \cdot 0047 \times \sqrt{(0 \cdot 24/0 \cdot 58)}]$, with suction through the full and the reduced areas respectively*. The Porosint areas used in the experiments and the experimental $C_Q$ values required are much larger than those estimated theoretically, but the velocity into the Porosint is in fair agreement with the theoretical estimate. Therefore, it seems likely that even lower values of $C_Q$ would suffice if the porous area were reduced further.

The flow over the aerofoil was investigated at incidences just below the stall. Both without suction and with suction, the flow separated on the upper surface of the nose but became re-attached some distance aft. The complete stall appeared to develop from rearward movement of the position of reattachment.

The slope of the experimental lift curves at *low* incidences, when reduced by the factor of 6 per cent to allow for wind-tunnel constraint (lift effect), is about $5 \cdot 3$ per radian, about 22 per cent lower than the theoretical value of $6 \cdot 8$.

The theoretical $M_{\text{crit}}$ of the H.S.A. V aerofoil without suction has the values $0 \cdot 68$ and $0 \cdot 52$ for the incidences of 0 deg and 2 deg respectively. However, as the theoretical velocity distributions consist of a peak at the nose followed by an almost constant velocity back to mid-chord, the effect of shock waves on the drag may not be marked until Mach numbers much higher than the $M_{\text{crit}}$ are reached (*see* R. & M. 2242[6]).

4. *Conventional Aerofoils with Slot Suction.*—The results from German tests on three moderately thick conventional aerofoils with slot suction are summarised in Table 1. The $C_{L\,\max}$ and $\alpha_{\max}$, for a given aerofoil and constant value of $C_Q$, vary extensively with the location of the slot on the upper surface, and the slot position giving the highest $C_{L\,\max}$ differs from that for the highest $\alpha_{\max}$†. The best position of the slot (either in respect of $C_{L\,\max}$ or $\alpha_{\max}$) is different for each aerofoil,

* From the experimental results, it appears that the $C_L$ without suction for $\alpha = 15$ deg decreases by $0 \cdot 06$ when $R$ is increased from $0 \cdot 24 \times 10^6$ to $0 \cdot 58 \times 10^6$; the difference between the $C_L$ with and without suction at a given incidence is assumed to be independent of $R$ provided $C_Q\sqrt{R}$ remains constant.

† It is relevant to note that, theoretically, the introduction of a sink on the upper surface increases the circulation (and hence lift) at a given incidence, by an amount which vanishes as the sink is placed closer to the leading edge.

being nearest the leading edge for the aerofoil with the smallest nose radius. It appears, from these tests, that a *large* nose radius is conducive to high $C_{L\,\max}$ and $\alpha_{\max}$ without suction, and to large increments by means of slot suction.

Fig. 9 shows the theoretical velocity distribution over the upper surface of H.S.A. V at a high incidence, when a sink of strength $C_Q = 0 \cdot 01$ is located at various positions on the upper surface of the nose. The velocity first rises from the stagnation point on the lower surface of the nose, but may fall again before ultimately rising to its infinite value at the sink. The magnitude of this velocity fall diminishes as the sink is placed closer to the leading edge and vanishes when the sink is very near to the leading edge. Immediately behind the sink there is a stagnation point. The velocity gradient is afterwards favourable for a short distance until a finite velocity maximum is reached, and then remains adverse right back to the trailing edge. The velocity fall, from the maximum to the value at the trailing edge, increases as the sink is placed nearer to the leading edge. Thus, in practice, a very careful choice of slot position is necessary so that the stall may be delayed to the highest possible incidence. The curves in Fig. 9 give a very rough idea of the gains feasible by slot suction on H.S.A. V. For example, the adverse velocity gradients over the upper surface at an incidence of $12 \cdot 7$ deg ($C_L = 1 \cdot 5$) and a sink strength $C_Q = 0 \cdot 01$ at $0 \cdot 006$ of the chord from the leading edge are clearly less severe than those for an incidence of $8 \cdot 7$ deg ($C_L = 1 \cdot 0$) and no sink action.

5. *Concluding Remarks*.—The Lighthill and the Glauert slot-suction aerofoils do not differ appreciably, either in their stalling characteristics (*see* Figs. 2 and 3) or in their velocity distributions at low incidences (*see* Fig. 6). The gains in $C_{L\,\max}$ and $\alpha_{\max}$ due to suction are poor, but the values of $C_{L\,\max}$ and $\alpha_{\max}$ without suction are quite high considering the steep fall in the theoretical velocity at the nose. The H.S.A. V aerofoil with distributed suction through the proper area of porous surface at the nose promises to be more economical than these slot-suction aerofoils as regards suction quantities for the postponement of the stall at full-scale Reynolds numbers. But this requires further confirmation by tests at high Reynolds numbers, and the respective power requirements also need investigation.

The thin slot-suction aerofoils already tested were specially designed to have, on the upper surface at high incidences, a large steep fall in velocity at the nose slot followed by a low steady adverse velocity gradient aft of the slot back to the trailing edge. For comparison, tests on a thin *conventional* aerofoil, with sink action at a nose slot to reduce the adverse velocity gradients at high incidences, would be very useful; the nose radius should be large and the slot position carefully chosen (*see* Section 4).

Some drag tests on thin nose-suction aerofoils at high speeds are also needed, as adverse effects on the drag due to the slot or to the porous surface may arise. Such effects may possibly be removed by a small amount of suction, in which case the economy of this procedure must be carefully considered.

For a fair assessment of the practical value of thin nose-suction aerofoils, their characteristics should be compared, in the first instance, with those of a thin conventional aerofoil incorporating a normal (non-suction) device at the nose to delay the stall to a higher incidence. Since nose devices usually have moveable parts and may lead to nose shapes which are poor from a low-drag standpoint, nose-suction aerofoils may be preferable for high speed aircraft. The use of nose-suction aerofoils, at the outboard sections of swept-back wings, is now being considered for the prevention of early tip-stalling. In this connection, tests under three-dimensional flow conditions (rather than two-dimensional) are of the utmost importance.

The maximum lift of thin nose-suction aerofoils may be further increased by the introduction of trailing-edge devices. It may be profitable, from this standpoint, for the air sucked in at the nose to be ejected downstream over a trailing-edge flap.

## PART II

# A Theoretical Investigation on Thin High-Lift Aerofoils Specially Designed for Nose-Slot Suction

6. *Introduction.*—A theoretical exploration of possible thin sections designed to have a large abrupt fall in velocity on the upper surface of the nose at high incidences has been carried out in an attempt to improve on the Lighthill and Glauert sections discussed in Part I.* Approximate theory has been employed to enable a comprehensive survey to be made fairly quickly. Various symmetrical 8 per cent thick shapes were first designed and the effect of camber was initially examined by adding a normal type centre-line. However, with such a centre-line, the aerofoil has an abrupt velocity fall on the lower surface, so new centre-lines were designed specially to eliminate this unnecessary and undesirable feature. The effect of a sink at the abrupt velocity fall was also investigated.

7. *Method of Design.*—The velocity $q$ over an aerofoil (expressed as a fraction of the free-stream velocity) may, on the basis of Goldstein's Approximation I, be expressed in the form[9]

$$q = 1 + g_s \pm \left[g_i + \frac{1}{2}\left(\frac{1}{a_0} + \frac{1}{2\pi}\right)\left(C_L - C_{L\,\mathrm{opt}}\right)\cot\tfrac{1}{2}\theta - \frac{1}{2}\left(\frac{1}{a_0} - \frac{1}{2\pi}\right)C_L\tan\tfrac{1}{2}\theta\right],$$

where the upper (positive) sign refers to the upper surface $(y_c + y_s)$ and the lower (negative) sign to the lower surface $(y_c - y_s)$, and where the chordwise co-ordinate $x = \frac{1}{2}(1 - \cos\theta)$ is measured from the leading edge. The contribution $1 + g_s$ corresponds to the velocity distribution over the fairing $\pm y_s$ at zero incidence, and is specified here to have a discontinuous fall at the point $x = X_1$ near the leading edge. The centre-line $y_c$ can be designed from a knowledge of $g_i$.

The velocity distributions chosen for the symmetrical sections at zero incidence, on the basis of Goldstein's Approximation I, are of the form shown in Fig. 10a. The velocity $q$ changes linearly from a value $1 + g_s(0)$ at the leading edge $(x = 0)$ to $1 + g_s(X_1)$ at $x = X_1$ where it drops discontinuously to $1 + g_s'(X_1)$; it then increases linearly to a value $1 + g_s(X_2)$ at $x = X_2$ and finally decreases to $1 + g_s(1)$ at the trailing edge. The formulae for calculating the section shape, and the functions arising in Goldstein's Approximations II and III for the velocity distributions, are derived in Appendix III.

Cambered shapes were in the first instance obtained by adding the simple centre-line[10] given in Table 4, which has a continuous $g_i$, has no negative loading, and has a low value $(-\frac{1}{8})$ for $C_{m0}/C_{L\,\mathrm{opt}}$. However, with such a centre-line, the section has an abrupt velocity fall on the lower surface. Clearly, for a continuous velocity distribution over the lower surface, $g_i$ must have a discontinuous fall at $x = X_1$ of the same magnitude as that for $g_s$. Four centre-lines for use with the most promising fairing shape (D.2) were later designed to have the required discontinuity in $g_i$ at $x = X_1$ and with $g_i$ linear in each of the two segments as illustrated in Fig. 10b. Formulae given in a comprehensive paper by Goldstein on the design of centre-lines[12] were employed to obtain their characteristics. Table 5 lists the basic-design data relating to these four centre-lines, together with the corresponding values obtained for $C_{m0}$.

8. *Aerofoil Section Characteristics.*—Various symmetrical shapes, of which the four shown in Fig. 11 are typical, were designed by the simple approximate method outlined in Section 7 and Appendix III. The parameter $g_s(X_2)$ controls primarily the maximum thickness; $g_s(1)$ is chosen to give a cusped trailing-edge, and $g_s(0)$, $g_s(X_1)$, $g_s'(X_1)$ determine primarily the shape

* It will be recalled that to prevent separation due to the abrupt velocity fall, the boundary layer is assumed to be removed through a narrow slot there; in addition, sink action at the slot may be used to reduce adverse velocity gradients in the vicinity of the nose.

of the forward part of the aerofoil. An increase in $g_s(0)$ or $g_s(X_1)$ increases $\rho_L$ and the nose thickness, but has little effect on the maximum thickness $t$ and its chordwise position ($x = x_t$) or on the trailing-edge shape. An increase in $g_s'(X_1)$ produces an overall thickening of the forward part of the aerofoil, so that $g_s(X_2)$ has to be decreased to keep $t$ constant, and $x_t$ is slightly reduced. Decrease of $X_2$ also leads to a reduction in $x_t$. Data relating to eleven symmetrical sections designed by this simple method are listed in Table 3. For the series A, $X_1 = 0 \cdot 005$ and $X_2 = 0 \cdot 35$; for the series B, $X_1$ remains unchanged but $X_2$ is decreased to $0 \cdot 25$; for the series C, D and E, $X_1$ takes the values $0 \cdot 003$, $0 \cdot 02$ and $0 \cdot 05$ respectively, and $X_2 = 0 \cdot 35$ as at first.

The type of velocity distribution obtained for these sections by means of Approximation III is illustrated in Fig. 10(c). The upper surface velocity distributions* for the symmetrical section A.2, as given by Approximations I, II, and III, are compared in Fig. 13, and it is seen that at high lifts Approximation II is insufficiently accurate over the nose. Table 6 lists the values of the maximum velocities $q_{\max}$ and $q'_{\max}$ in front of and behind the discontinuity, and the values $q_1$ and $q_1'$ of the velocity at the discontinuity, calculated by means of Approximation III, for the eleven symmetrical sections at various lift coefficients. Fig. 14 shows the velocity distributions for the four symmetrical sections A.2, A.5, D.2 and E.1 (*see* Fig. 11) at $C_L = 0$ and $C_L = 1 \cdot 0$.

Table 7 gives the values of $q_{\max}$, $q'_{\max}$, $q_1$, and $q_1'$ for the four cambered sections A.2/N, A.5/N, D.2/N, and E.1/N obtained by adding the normal-type centre-line of Table 4 to the fairing shapes A.2, A.5, D.2, and E.1 respectively, and for the four cambered sections D.2/1, D.2/2, D.2/3, and D.2/4 (*see* Fig. 12) obtained by adding the discontinuous-type centre-lines of Table 5 to the fairing shape D.2.

The effect of a sink, located at the upper surface velocity discontinuity, on the velocity distributions at high lifts is illustrated in Fig. 10d. The velocity first rises from a zero value at the stagnation point on the lower surface of the nose to a maximum value $q_{\max}$ on the upper surface of the nose but may fall again to a minimum $q_{\min}$ before ultimately rising to its infinite value at the sink. Immediately behind the sink there is a stagnation point, aft of which the velocity gradient is favourable for a short distance until a maximum value $q'_{\max}$ is reached, and then remains adverse right back to the trailing-edge. Table 8 gives the values of $q_{\max}$, $q_{\min}$ and $q'_{\max}$ for the four symmetrical sections of Fig. 11, with a sink ($C_Q = 0 \cdot 003$†) at the discontinuity, and Table 9 gives the corresponding values for the cambered versions already mentioned.

9. *Analysis of Results.*—In a discussion of the stalling properties, it is important to observe that, at high incidences, adverse velocity gradients may appear on the upper surface ahead of the discontinuity as well as behind. Again, in relation to the high-speed performance at low incidences, it should be noted that the velocities ahead of the discontinuity may be very large.

*Effect of Changes in Fairing Shape on the Upper Surface Velocity Distribution.* (*See* Tables 3 and 6, Figs. 11 and 14). A larger $\varrho_L$ with a more marked concavity near the discontinuity (*cf.* sections A.2 and A.5) improves the velocity gradients at high incidences, both in front of and behind the discontinuity. At low incidences, the velocity gradients ahead of the maximum thickness become more favourable; the maximum velocity behind the discontinuity is little changed, but the value in front of the discontinuity is considerably increased.

Forward movement of the position of maximum thickness with a general fattening of the forward part of the section (*cf.* A.2, A.4 and A.6) improves the velocity gradients ahead of the discontinuity at high incidences, but has little effect on those behind the discontinuity. However, at low incidences, the maximum velocity behind the discontinuity is increased and is located further forward, so that the region of adverse velocity gradients becomes more extensive.

* Attention will be restricted here to the upper surface velocity distributions, as at high lifts the velocity gradients on the *lower* surface will be favourable everywhere except possibly at the lower surface velocity discontinuity.

† This is the practical value envisaged for wings of this thickness.

Rearward movement of the position of the discontinuity without marked alteration in the general section shape, improves the velocity gradients behind the discontinuity at high incidences, at the expense of those in front (*cf.* A.2 and D.1). These latter gradients can be restored to some extent by increasing $\varrho_L$ as already mentioned (*cf.* A.2 and A.5, D.1 and D.2).

*Comparison of Maximum Lift Properties.*—The maximum lifts of these sections are very difficult to estimate theoretically, especially since the boundary-layer separation may arise before or after the discontinuity, and a reattachment may also occur. For a rough but quick comparison of probable maximum lift properties, an upper limit $C_{L\,\mathrm{lim}}$ to the lift coefficient has been chosen, at which the maximum velocity $q'_{\mathrm{max}}$ behind the upper surface discontinuity does not exceed twice the free-stream velocity* and the velocity gradients in front of the discontinuity are still favourable. Table 10, derived with the aid of Fig. 15, gives the values of $C_{L\,\mathrm{lim}}$ for the four symmetrical shapes A.2, A.5, D.2 and E.1 shown in Fig. 11, for the four cambered versions of these sections with the normal-type centre-line, and for the Lighthill section, both without and with a sink ($C_Q = 0{\cdot}003$) at the discontinuity on the upper surface. It is evident from Fig. 15 that the values of $C_{L\,\mathrm{lim}}$ for the sections with the fairing shapes A.2 and A.5 and for the Lighthill are in fact limited by the first condition, $q'_{\mathrm{max}} \leqslant 2$, while the values for the sections with the fairing shapes D.2 and E.1 are limited by the second condition which requires favourable gradients ahead of the discontinuity.

The values of $C_{L\,\mathrm{lim}}$ for the four cambered sections D.2/1, D.2/2, D.2/3, and D.2/4, with the fairing shape D.2 and discontinuous type centre-lines are $2{\cdot}1$, $1{\cdot}9$, $2{\cdot}0$, and $1{\cdot}8$, respectively, as compared with the value $1{\cdot}3$ for the Lighthill section. With these five sections the theoretical velocity gradients ahead of the discontinuity remain favourable for all the high-lift conditions considered, so that $C_{L\,\mathrm{lim}}$ is essentially limited by the condition $q'_{\mathrm{max}} \leqslant 2$.† The increments of $C_{L\,\mathrm{lim}}$ obtained with a sink ($C_Q = 0{\cdot}003$) at the discontinuity are less than $0{\cdot}1$ for all five sections, *i.e.*, less than half the increment obtained with the sink on the fairing shape D.2 alone (*see* Table 10).

*Drags at High Speeds.*—A comparison of the drags of these sections at high speeds is not possible at present. The velocity in a very *small* region ahead of the discontinuity is considerably larger than the maximum velocity behind the discontinuity (*see* Figs. 14 and 16). The region increases in extent as the discontinuity is moved further rearward, and may be important from shock-wave considerations.

10. *Conclusions.*—The comparison of maximum lift properties made in section 9 indicates that the stalling incidences and maximum lifts for the cambered versions of the D.2 shape should be considerably larger than those for the Lighthill section, at practical suction quantities. The improvement has been obtained by moving the suction slot back to $0{\cdot}02c$ from the leading edge and increasing $\varrho_L$ to $0{\cdot}02c$. Of the four cambered sections with the velocity discontinuity on the lower surface removed, the section D.2/4 is probably the most acceptable from pitching moment and high speed considerations, although it is the least promising as far as maximum lift is concerned. Low-speed stalling tests are to be made on this section to determine whether the considerable improvements expected are in fact achieved. If the results are satisfactory the effect of the unusual nose shape on the high-speed performance of this type of section will need to be investigated experimentally.

---

* The maximum velocity $q'_{\mathrm{max}}$ provides a measure of the severity of the adverse velocity gradients behind the discontinuity.

† This suggests that, for cambered sections with a velocity discontinuity on the upper surface only, the position of the discontinuity might with slight advantage be taken a little further back than $0{\cdot}02c$ from the leading edge, since the velocity gradients behind the discontinuity would then be improved at the expense of those in front.

## APPENDIX I

### *Theoretical Formulæ for the Effect of a Sink on an Aerofoil*

Theoretical formulæ are derived for the velocity distribution and lift of an aerofoil with a sink on its surface, when the aerofoil is designed by the exact and approximate methods respectively.

The region outside the aerofoil, in the $z(\equiv x + iy)$ plane, is obtained by a conformal transformation from the region outside a circle $\zeta = Re^{i\phi}$, so that $d\zeta/dz \longrightarrow 1$ as $|\zeta| \longrightarrow \infty$, and so that one particular point on the aerofoil corresponds to a chosen point on the circle. Consider the flow past the circle, with a stream of unit velocity at incidence $\alpha$, with a sink of strength $2\pi m$ on the circle at $\phi = \beta$, and with circulation $2\pi\varkappa$, as indicated in the diagram below.

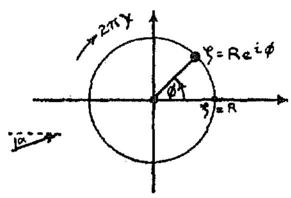


If $\hat{q}_{am}$ denotes the velocity at the circle boundary, it is readily shown that

$$\hat{q}_{am} = \left| 2\sin(\phi - \alpha) + \frac{\varkappa}{R} + \frac{m}{R}\cot\tfrac{1}{2}(\phi - \beta) \right| . \quad \ldots \quad (AI.1)$$

The corresponding velocity over the aerofoil surface will be denoted by $q_{am}$.

In the exact method of design[7, 8], the radius $R$ is chosen as unity, and the trailing edge of the aerofoil is taken to correspond to the point $\zeta = 1$ on the circle. When the circulation is adjusted so that $\zeta = 1$ is a stagnation point,

$$\varkappa = 2\sin\alpha + m\cot\tfrac{1}{2}\beta\,,$$

and

$$\hat{q}_{am} = |\, 4\sin\tfrac{1}{2}\phi\cos(\tfrac{1}{2}\phi - \alpha) + m\,\mathrm{cosec}\,\tfrac{1}{2}\beta\sin\tfrac{1}{2}\phi\,\mathrm{cosec}\,\tfrac{1}{2}(\phi - \beta)\,| \,.$$

It follows that

$$q_{am}/q_{00} = \left| \frac{\cos(\tfrac{1}{2}\phi - \alpha)}{\cos\tfrac{1}{2}\phi} + \frac{m}{4}\,\mathrm{cosec}\,\tfrac{1}{2}\beta\,\mathrm{cosec}\,\tfrac{1}{2}(\phi - \beta)\sec\tfrac{1}{2}\phi \right| \quad \ldots \quad (AI.2)$$

and the lift coefficient of the aerofoil is

$$C_{Lm} = \frac{4\pi}{c_0}(2\sin\alpha + m\cot\tfrac{1}{2}\beta)\,, \quad \ldots \quad (AI.3)$$

where $c_0$ denotes the aerofoil chord corresponding to the unit circle ; $\alpha$ represents the angle of incidence measured from the zero-lift attitude without suction. In the design calculations, $q_{00}$ and the co-ordinates $x, y$ are tabulated at convenient intervals of $\theta$, and $c_0$ is also determined.

In Goldstein's approximate method of design[9], the co-ordinates of the aerofoil are usually expressed as

$$x = \tfrac{1}{2}(1 - \cos\theta), \quad y = \tfrac{1}{2}\psi\sin\theta\,, \quad \ldots \quad (AI.4)$$

where the trailing edge corresponds to $\theta = \pi$. The angular co-ordinate $\phi$ on the circle is then $\pi - (\theta + \varepsilon)$, where $\varepsilon$ is a function of $\theta$; the radius of the circle will be denoted as $R_0$. If, when $\phi = \beta$, $\theta = \eta$ and $\varepsilon = \varepsilon_\eta$, then from equation (AI.1)

$$\hat{q}_{am} = \left| 2 \sin(\theta + \alpha + \varepsilon) + \frac{\varkappa}{R_0} - \frac{m}{R_0} \cot \tfrac{1}{2}(\theta + \varepsilon - \eta - \varepsilon_\eta) \right| .$$

If the circulation is adjusted so that the point on the circle given by $\theta = \pi$ becomes a stagnation point, then

$$\frac{\varkappa}{R_0} = 2 \sin(\alpha + \varepsilon_\pi) + \frac{m}{R_0} \cot \tfrac{1}{2}(\pi + \varepsilon_\pi - \eta - \varepsilon_\eta)$$

where $\varepsilon_\pi$ is the value of $\varepsilon$ for $\theta = \pi$. Thus, here, the incidence measured from the zero-lift attitude (without suction) is $\alpha + \varepsilon_\pi$.

It is customary, in the approximate method of design, to write $|d\zeta/dz| = \frac{1}{2}F(\theta)$ for points on the circle, and so

$$\begin{aligned} q_{am} &= |d\zeta/dz| \; \hat{q}_{am} \\ &= F(\theta) \Big| \sin(\theta + \alpha + \varepsilon) + \sin(\alpha + \varepsilon_\pi) \\ &\qquad - \frac{m}{2R_0} \left\{ \cot \tfrac{1}{2}(\theta + \varepsilon - \eta - \varepsilon_\eta) - \cot \tfrac{1}{2}(\pi + \varepsilon_\pi - \eta - \varepsilon_\eta) \right\} \Big| . \end{aligned} \qquad \text{(AI.5)}$$

The lift coefficient of the aerofoil is

$$C_{Lm} = 4\pi R_0 \left[ 2 \sin(\alpha + \varepsilon_\pi) + \frac{m}{R_0} \cot \tfrac{1}{2}(\pi + \varepsilon_\pi - \eta - \varepsilon_\eta) \right] . \qquad \text{(AI.6)}$$

Now we may write $C_{L0}/a_0 = \sin(\alpha + \varepsilon_\pi)$ where $C_{L0}$ represents the lift coefficient for zero $m$ and where $a_0 = 8\pi R_0$. Furthermore,

$$\begin{aligned} \sin(\theta + \alpha + \varepsilon) &= \sin(\alpha + \varepsilon_\pi) \cos(\theta + \varepsilon - \varepsilon_\pi) + \cos(\alpha + \varepsilon_\pi) \sin(\theta + \varepsilon - \varepsilon_\pi) \\ &= \frac{C_{L0}}{a_0} \cos(\theta + \varepsilon - \varepsilon_\pi) + \left(1 - \frac{C_{L0}{}^2}{a_0{}^2}\right)^{1/2} \sin(\theta + \varepsilon - \varepsilon_\pi). \end{aligned}$$

The relations (AI.5) and (AI.6) then become

$$\begin{aligned} q_{am} = F(\theta) \Big| &\left(1 - \frac{C_{L0}{}^2}{a_0{}^2}\right)^{1/2} \sin(\theta + \varepsilon - \varepsilon_\pi) + \frac{C_{L0}}{a_0} \cos(\theta + \varepsilon - \varepsilon_\pi) + \frac{C_{L0}}{a_0} \\ &- \frac{m}{2R_0} \left\{ \cot \tfrac{1}{2}(\theta + \varepsilon - \eta - \varepsilon_\eta) - \cot \tfrac{1}{2}(\pi + \varepsilon_\pi - \eta - \varepsilon_\eta) \right\} \Big| \end{aligned} \qquad \text{(AI.7)}$$

and

$$C_{Lm} = C_{L0} + 4\pi m \cot \tfrac{1}{2}(\pi + \varepsilon_\pi - \eta - \varepsilon_\eta) . \qquad \text{(AI.8)}$$

In the design calculations, $\varepsilon$ and $F(\theta)$ are tabulated at convenient intervals of $\theta$, and $a_0 = 8\pi R_0$ is determined. Actually, $4R_0 \simeq 1$, so that $m/2R_0 = 2\pi m/4\pi R_0 \simeq C_Q/\pi$ in equation (AI.7)

## *APPENDIX II*

### *The Glauert Nose-Slot Suction Aerofoil*

The design of the Glauert nose-slot suction aerofoil has not previously been reported in detail, but will be presented here*. The exact method[7,8], extended to enable the slot shape to be incorporated automatically in the aerofoil, was used. In the following discussion, some of the formulae derived in Appendix I, for the exact method, will be required.

The formulae for the aerofoil co-ordinates $(x, y)$ are

$$x = \int (2 \sin \phi / q_{00}) \cos \chi \, d\phi, \quad y = \int (2 \sin \phi / q_{00}) \sin \chi \, d\phi, \text{ where}$$

$$x(\phi) = (1/2\pi) \, P \int_{-\pi}^{\pi} \log q_{00}(t) \cot \tfrac{1}{2}(\phi - t) \, dt$$

is the function conjugate to $\log q_{00}(\phi)$. The function $\log q_{00}$ must satisfy the relations

$$\int_{-\pi}^{\pi} \log q_{00} \, d\phi = 0, \int_{-\pi}^{\pi} \log q_{00} \cos \phi \, d\phi = 0, \int_{-\pi}^{\pi} \log q_{00} \sin \phi \, d\phi = 0. \quad \ldots \quad \ldots \quad \ldots \quad \text{(AII.1)}$$

It is usually expressed in terms of the velocity over the upper surface at an upper design incidence $\alpha_1$, and over the lower surface at a lower design incidence $\alpha_2$; the necessary relations are provided by the equation (AI.2), when a sink is assumed to lie at $\phi = \beta$. If the sink strength is such that, at incidence $\alpha$, there is a stagnation point on the circle at $\phi = \beta - \gamma$, equation (AI.2) reduces to

$$\frac{q_{\alpha m}}{q_{00}} = \left| \frac{\sin \frac{1}{2}(\phi - \beta + \gamma) \cos \frac{1}{2}(\phi - \gamma - 2\alpha)}{\sin \frac{1}{2}(\phi - \beta) \cos \frac{1}{2}\phi} \right| . \quad \ldots \quad \ldots \quad \ldots \quad \ldots \quad \text{(AII.2)}$$

Furthermore, if the strength is adjusted so that $\gamma$ remains constant as $\alpha$ is varied, then

$$\frac{q_{\alpha m}}{q_{00}} = \left| \frac{\cos \frac{1}{2}(\phi - \gamma - 2\alpha)}{\cos \frac{1}{2}(\phi - \gamma)} \right| . \quad \ldots \quad \ldots \quad \ldots \quad \ldots \quad \ldots \quad \ldots \quad \ldots \quad \text{(AII.3)}$$

The velocity over the aerofoil may be specified to be finite and continuous everywhere. A shaped slot is then obtained on the aerofoil of width equal to the sink strength divided by the velocity on the aerofoil at $\phi = \beta$†.

The velocity distribution was chosen by Glauert to be of the form (with $\alpha_2 = 0$)

$$\left.\begin{array}{lll}
\log q_{0m} = & \log | \cos \frac{1}{2}(\phi - \gamma)/\cos \frac{1}{2}(\phi - \gamma - 2\alpha_1)| \quad \ldots & \gamma + \alpha_1 < \phi < \pi + \gamma + \alpha_1 \\
& + l + a(1 - \cos \phi) \quad \ldots \quad \ldots \quad \ldots \quad \ldots & 0 < \phi < \beta \\
& + l + b(1 - \cos \phi) \ldots \quad \ldots \quad \ldots \quad \ldots \quad \ldots & \beta < \phi < 2\pi \\
& + c(\sin \overline{\beta - \gamma} - \sin \phi) \quad \ldots \quad \ldots \quad \ldots \quad \ldots & \beta - \gamma < \phi < \beta \\
& + d(\sin \overline{\alpha_1 + \gamma} + \sin \phi) \quad \ldots \quad \ldots \quad \ldots & \pi + \delta < \phi < \pi + \alpha_1 + \gamma \\
& + d(\sin \overline{\alpha_1 + \gamma} - \sin \delta) \quad \ldots \quad \ldots \quad \ldots \quad \ldots & \beta < \phi < \pi + \delta \\
& + g \cos 3\phi \quad \ldots \quad \ldots \quad \ldots \quad \ldots \quad \ldots \quad \ldots & \pi/2 < \phi < \beta
\end{array}\right\} \quad \text{(AII.4)}$$

From equation (AII.2), we have also

$$\log q_{00} = \log \left| \frac{\sin \frac{1}{2}(\phi - \beta) \cos \frac{1}{2}\phi}{\sin \frac{1}{2}(\phi - \beta - \gamma) \cos \frac{1}{2}(\phi - \gamma)} \right| + \log q_{0m} \quad \ldots \quad \ldots \quad \ldots \quad \text{(AII.5)}$$

---

* The writer gratefully acknowledges information and advice received from Mr. M. B. Glauert concerning the design of this aerofoil.

† In the integration to obtain the aerofoil shape, it is necessary to check, not that the contour closes up, but that there is a slot entry of the correct width; the sides of the slot approach assymptotically to the same direction at a constant width apart.

In view of the relation (AII.3), log $q_{\alpha_1 m}$ and log $q_{0m}$ are given over the ranges $\gamma + \alpha_1 < \phi < \pi + \gamma + \alpha_1$ and $\pi + \gamma + \alpha_1 < \phi < 2\pi + \gamma + \alpha_1$ respectively, by ignoring the log term in the expression (AII.4) for log $q_{0m}$. The purpose of the remaining terms is now briefly explained.

The terms involving the constants $l$, $a$ and $b$ provide steadily falling velocities over the upper surface at incidence $\alpha_1$, and over the lower surface at zero incidence. The $c$ term gives a rising velocity from the slot lip (at $\phi = \beta - \gamma$) into the slot (at $\phi = \beta$), and $c$ is chosen so that log $q_{am}$ is continuous at $\phi = \beta$. The $d$ terms give a high and non-decreasing velocity from the front stagnation point to the slot at incidence $\alpha_1$; $d$ is chosen to make $d/d\phi$ (log $q_{am}$) continuous at $\phi = \pi + \gamma + \alpha_1$ and $\delta$ is chosen to provide a velocity of suitable magnitude. Finally, the constant $g$ may be arbitrarily assigned a negative constant value to increase $M_{\text{crit}}$ at low incidence, but the adverse velocity gradients at high incidence are simultaneously worsened. When $\alpha_1$, $\beta$, $\gamma$, $\delta$ and $g$ are assigned, the values of $l$, $a$, $b$, $c$ and $d$ may be obtained from the three conditions (AII.1) together with the two supplementary conditions given above.

Glauert eventually chose $\alpha = 12$ deg, $\beta = 174$ deg, $\gamma = 0$ deg 4 min, $\delta = 4$ deg and $g = -0{\cdot}065$, which yielded the values $l = -0{\cdot}0713061$, $a = 0{\cdot}3693949$, $b = 0{\cdot}1267340$, $c = 699{\cdot}5190$, $d = 9{\cdot}729334$. The aerofoil co-ordinates and the values of the design velocities $q_{0m}$ and $q_{00}$ are set out in Table 2. It is relevant to note that the sink strength chosen gave a slot width far too small for the suction quantities used in the experimental tests.

---

## *APPENDIX III*

### *Design Formulae for the Symmetrical Sections*

The velocity distribution for a symmetrical aerofoil at zero incidence to the airstream may be expressed, on the basis of Goldstein's Approximation I, in the form[9]

$$q = 1 + g_s$$

where the chordwise co-ordinate $x = \frac{1}{2}(1 - \cos\theta)$ is measured from the leading edge. In the following analysis, $g_s$ is assumed to increase linearly with $x$ in any segment $\theta_{r-1} < \theta < \theta_r$, from the value $g_s'(X_{r-1})$ at $\theta = \theta_{r-1}$ to the value $g_s(X_r)$ at $\theta = \theta_r$, where $g_s(X_r)$ and $g_s'(X_r)$ are not necessarily identical. Thus, for $\theta_{r-1} < \theta < \theta_r$,

$$g_s = \frac{\{-g_s'(X_{r-1})\cos\theta_r + g_s(X_r)\cos\theta_r\}}{(\cos\theta_{r-1} - \cos\theta_r)} + \frac{\{g_s'(X_{r-1}) - g_s(X_r)\}}{(\cos\theta_{r-1} - \cos\theta_r)}\cos\theta \qquad \text{..(AIII.1)}$$

Let $M_{0r}$ be a generic symbol to represent the contributions to the functions $2y_s$, $G(\theta) = \int_0^\theta g_s \sin\theta \, d\theta$, and to the constants $(2\varrho_L)^{1/2}$, $(2\varrho_T)^{1/2}$, $C_0$, when $g_s = 1$ for $\theta_{r-1} < \theta < \theta_r$*. Similarly, let $M_{1r}$ be the corresponding generic symbol when $g_s \equiv \cos\theta$ for $\theta_{r-1} < \theta < \theta_r$. The formulae giving the values of these contributions have already been derived in section 3 of Ref. 11. Summing over the several segments which constitute the whole range $0 < \theta < \pi$, $r = 1$ to $n$ say, we have

$$2\pi y_s, \text{ etc.} = \sum_r \left\{ \frac{-\cos\theta_r M_{0r} + M_{1r}}{\cos\theta_{r-1} - \cos\theta_r} g_s'(X_{r-1}) + \frac{\cos\theta_{r-1} M_{0r} - M_{1r}}{\cos\theta_{r-1} - \cos\theta_r} g_s(X_r) \right\}. \qquad \text{(AIII.2)}$$

The remaining functions required for Approximation III then follow from the relations

$$\varepsilon_s(\theta) = G(\theta)\operatorname{cosec}\theta - C_0 \tan\tfrac{1}{2}\theta, \qquad \text{.. .. .. .. .. .. (AIII.3)}$$

* Note that the contributions themselves are not restricted merely to the range $\theta_{r-1} < \theta < \theta_r$.

$$\left.\begin{aligned} \frac{d\varepsilon_s(\theta)}{d\theta} &= g_s - \frac{G(\theta)\cos\theta}{\sin^2\theta} - \frac{C_0}{1+\cos\theta} \\ d\varepsilon_s(\theta)/d\theta = \tfrac{1}{2}\{g_s'(0) - C_0\}&,\ d\varepsilon_s(\pi)/d\theta = \tfrac{1}{2}\{g_s(X_n) - C_0\} \end{aligned}\right\} \quad \ldots \quad (AIII.4)$$

For the symmetrical sections considered in the main text, $n = 3$, and $g_s(X_r) = g_s'(X_r)$, except when $r = 1$.

*Acknowledgment*.—The writer is indebted to Miss E. M. Love of the Aerodynamics Division, N.P.L., for her assistance with the computational work and the preparation of diagrams for this report.

---

## REFERENCES


| *No.* | *Author* | *Title, etc.* |
|---|---|---|
| 1 | F. Cheers, W. G. Raymer and O. Douglas | Tests on a 'Lighthill' Nose-suction Aerofoil in the N.P.L. 4 ft, No. 2 Wind Tunnel. R. & M. 2355. April, 1947. |
| 2 | F. Cheers and O. Douglas .. .. | Tests on a 'Glauert' Nose-suction Aerofoil in the N.P.L. 4 ft, No. 2 Wind Tunnel. R. & M. 2356. April, 1947. |
| 3 | R. C. Pankhurst, W. G. Raymer and A. N. Devereux | Wind Tunnel Tests of the Stalling Properties of an 8 per cent Thick Symmetrical Section with Continuous (Distributed) Nose Suction. A.R.C. 11,496. June, 1948. (To be published.) |
| 4 | A. Walz .. .. .. .. .. | Measurements for Increasing the Safety from Stalling by Sucking at the Front Part of the Profile. A.V.A. Gottingen Report No. 45/W/14. A.R.C. 10,050. October, 1945. |
| 5 | M. J. Lighthill .. .. .. .. | A Theoretical Discussion of Wings with Leading-edge Suction. R. & M. 2162. May, 1945. |
| 6 | B. Thwaites .. .. .. .. | A Theoretical Discussion of High-Lift Aerofoils with Leading-edge Porous Suction. A.R.C. 9809. R. & M. 2242. July, 1946. |
| 7 | M. J. Lighthill .. .. .. .. | A New Method of Two-dimensional Aerodynamic Design. R. & M. 2112. April, 1945. |
| 8 | M. B. Glauert .. .. .. .. | The Application of the Exact Method of Aerofoil Design. A.R.C. 10,933. October, 1947. (To be published.) |
| 9 | S. Goldstein .. .. .. .. | Low Drag and Suction Aerofoils. *J. Ae. Sc.* Vol. 15, p. 189. April, 1948. |
| 10 | Ola Douglas .. .. .. .. | A Series of Low Drag Aerofoils Embodying a New Camber-line. R. & M. 2494. May, 1947. |
| 11 | S. Goldstein .. .. .. .. | A Theory of Aerofoils of Small Thickness. Part III. Approximate Designs of Symmetrical Aerofoils for Specified Pressure Distributions. A.R.C. 6225. October, 1942. (To be published.) |
| 12 | S. Goldstein .. .. .. .. | Approximate Two-dimensional Aerofoil Theory. Part IV. The Design of Centre Lines. A.R.C. C.P.71. March, 1945. |

## TABLE 1

*Some Data from Tests on Aerofoils with Nose-Slot Suction*

| | Data \ Aerofoil | NACA 23015 | NACA 0015 | Bis 2315 | Lighthill | Glauert |
|---|---|---|---|---|---|---|
| Profile (unit chord) | Maximum Thickness .. .. .. | 0·15 | 0·12 | 0·12 | 0·086 | 0·086 |
| | Position of Max. Th. .. .. | 0·30 | 0·30 | 0·50 | 0·29 | 0·30 |
| | Nose Radius .. .. .. .. | 0·0248 | 0·0158 | 0·003 | Beaked Nose | small |
| | Camber .. .. .. .. | 0·02 | 0 | 0·021 | 0·018 | 0·019 |
| | Position of Max. Cam. .. .. | 0·15 | — | 0·50 | 0·35 | 0·48 |
| Max. Lift | $C_{L\ \max}$ for $C_Q = 0$ .. .. .. | 1·23 | 1·02 | 0·68 | 1·12 | 1·13 |
| | Optimum slot position .. .. | 0·20 | 0·10 | $\simeq$ 0·01 | — | — |
| | $\Delta\ C_{L\ \max}$, $C_Q = 0{\cdot}0025$ .. .. | 0·40 | 0·25 | 0 | | 0·19 |
| | $\Delta\ C_{L\ \max}$, $C_Q = 0{\cdot}0075$ .. .. | 0·95 | 0·56 | 0·23 | $\simeq$ 0·25 | $\simeq$ 0·25 |
| Max. Incidence | $\alpha_{\max}$, $C_Q = 0$ .. .. .. .. | 13·6 deg | 11·8 deg | 10·0 deg | 13·5 deg | 12·5 deg |
| | Optimum slot position .. .. | 0·17 | 0·03 | 0 | — | — |
| | $\Delta\ \alpha_{\max}$, $C_Q = 0{\cdot}0025$ .. .. | 8·0 deg | 1·8 deg | 0·7 deg | | $\simeq$ 1 deg |
| | $\Delta\ \alpha_{\max}$, $C_Q = 0{\cdot}0075$ .. .. | 12·5 deg | 4·0 deg | 2·5 deg | $\simeq$ 2 deg | $\simeq$ 2 deg |

TABLE 2

*Data for Glauert Nose-Slot Aerofoil*

| $\phi$ deg | $\phi$ min | Co-ordinates $x$ | Co-ordinates $y$ | Velocity (Zero Incidence) $q_{0m}$ | Velocity (Zero Incidence) $q_{00}$ |
|---|---|---|---|---|---|
| 0 | | 1·00000 | 0 | 0·93118 | 0·93121 |
| 10 | | 0·99145 | 0·00050 | 0·93642 | 0·93645 |
| 20 | | 0·96598 | 0·00226 | 0·93837 | 0·93840 |
| 30 | | 0·92459 | 0·00582 | 0·94650 | 0·94653 |
| 40 | | 0·86928 | 0·01172 | 0·96359 | 0·96362 |
| 50 | | 0·80268 | 0·01982 | 0·98844 | 0·98848 |
| 60 | | 0·72779 | 0·02962 | 1·02008 | 1·02012 |
| 70 | | 0·64764 | 0·03997 | 1·05678 | 1·05683 |
| 80 | | 0·56514 | 0·04959 | 1·09647 | 1·09653 |
| 90 | | 0·48308 | 0·05668 | 1·13616 | 1·13623 |
| 100 | | 0·40217 | 0·05978 | 1·13459 | 1·13468 |
| 110 | | 0·32332 | 0·05976 | 1·13362 | 1·13373 |
| 120 | | 0·24939 | 0·05722 | 1·13516 | 1·13531 |
| 130 | | 0·18282 | 0·05210 | 1·13455 | 1·13477 |
| 140 | | 0·12537 | 0·04427 | 1·11781 | 1·11815 |
| 150 | | 0·07806 | 0·03368 | 1·05874 | 1·05935 |
| 160 | | 0·04104 | 0·02104 | 0·91459 | 0·91592 |
| 162 | | 0·03484 | 0·01839 | 0·87009 | 0·87173 |
| 164 | | 0·02902 | 0·01574 | 0·81877 | 0·82085 |
| 166 | | 0·02355 | 0·01314 | 0·75975 | 0·76251 |
| 168 | | 0·01842 | 0·01063 | 0·69197 | 0·69589 |
| 170 | | 0·01359 | 0·00830 | 0·61420 | 0·62048 |
| 172 | | 0·00900 | 0·00633 | 0·52490 | 0·53852 |
| 172 | 20 | 0·00825 | 0·00607 | 0·50877 | 0·52540 |
| 172 | 40 | 0·00751 | 0·00584 | 0·49226 | 0·51351 |
| 173 | | 0·00678 | 0·00565 | 0·47536 | 0·50451 |
| 173 | 20 | 0·00606 | 0·00552 | 0·45805 | 0·50390 |
| 173 | 40 | 0·00538 | 0·00549 | 0·44033 | 0·54469 |
| 173 | 44 | 0·00526 | 0·00550 | 0·43674 | 0·57620 |
| 173 | 48 | 0·00515 | 0·00551 | 0·43313 | 0·64275 |
| 173 | 52 | 0·00506 | 0·00553 | 0·42950 | 0·84977 |
| 173 | 56 | 0·00502 | 0·00555 | 0·42585 | $\infty$ |
| 174 | | | | 0·94850 | 0 |

TABLE 2—*continued*

*Data for Glauert Nose-slot Aerofoil*

| $\phi$ deg | $\phi$ min | Co-ordinates $x$ | Co-ordinates $y$ | Velocity (Zero Incidence) $q_{0m}$ | Velocity (Zero Incidence) $q_{00}$ |
|---|---|---|---|---|---|
| 174 | 4 | 0·00472 | 0·00535 | 0·94013 | 0·46485 |
| 174 | 8 | 0·00461 | 0·00537 | 0·93173 | 0·61422 |
| 174 | 12 | 0·00451 | 0·00538 | 0·92330 | 0·68460 |
| 174 | 16 | 0·00442 | 0·00538 | 0·91482 | 0·72345 |
| 174 | 20 | 0·00434 | 0·00538 | 0·90631 | 0·74648 |
| 174 | 40 | 0·00396 | 0·00533 | 0·86318 | 0·77502 |
| 175 | | 0·00361 | 0·00522 | 0·81908 | 0·75779 |
| 175 | 20 | 0·00329 | 0·00509 | 0·77396 | 0·72673 |
| 175 | 40 | 0·00299 | 0·00493 | 0·72779 | 0·68920 |
| 176 | | 0·00270 | 0·00475 | 0·68054 | 0·64780 |
| 178 | | 0·00133 | 0·00339 | 0·37202 | 0·35412 |
| 180 | | 0·00042 | 0·00195 | 0·01298 | 0 |
| 182 | | 0·00001 | +0·00035 | 0·41009 | 0·42073 |
| 184 | | 0·00009 | −0·00104 | 0·91615 | 0·92552 |
| 186 | | 0·00039 | −0·00245 | 1·09265 | 1·09883 |
| 188 | | 0·00226 | −0·00379 | 1·17068 | 1·17493 |
| 190 | | 0·00415 | −0·00529 | 1·19485 | 1·19789 |
| 200 | | 0·02210 | −0·01308 | 1·19067 | 1·19161 |
| 210 | | 0·05388 | −0·01964 | 1·17961 | 1·18006 |
| 220 | | 0·09849 | −0·02451 | 1·16476 | 1·16503 |
| 230 | | 0·15507 | −0·02751 | 1·14670 | 1·14688 |
| 240 | | 0·22156 | −0·02829 | 1·12614 | 1·12627 |
| 250 | | 0·29679 | −0·02711 | 1·10382 | 1·10392 |
| 260 | | 0·37862 | −0·02427 | 1·08051 | 1·08059 |
| 270 | | 0·46482 | −0·02020 | 1·05699 | 1·05705 |
| 280 | | 0·55291 | −0·01547 | 1·03399 | 1·03404 |
| 290 | | 0·64019 | −0·01067 | 1·01216 | 1·01220 |
| 300 | | 0·72381 | −0·00634 | 0·99209 | 0·99213 |
| 310 | | 0·80086 | −0·00292 | 0·97430 | 0·97434 |
| 320 | | 0·86854 | −0·00066 | 0·95920 | 0·95923 |
| 330 | | 0·92424 | +0·00044 | 0·94712 | 0·94715 |
| 340 | | 0·96574 | 0·00060 | 0·93832 | 0·93835 |
| 350 | | 0·99135 | 0·00026 | 0·93297 | 0·93300 |
| 360 | | 1·00000 | 0 | 0·93118 | 0·93121 |

# TABLE 3

*Design and Shape Data of Symmetrical Sections*

| Section No. | Design data | | | | | | | Max. thickness | Position of max. thickness | Position of slot | $\varrho_L$ | Thickness at $x = X_1$ |
|---|---|---|---|---|---|---|---|---|---|---|---|---|
| | $X_1$ | $X_2$ | $g_s'(0)$ | $g_s(X_1)$ | $g'_s(X_1)$ | $g_s(X_2)$ | $g_s(1)$ | | | | | |
| A.1 | 0·005 | 0·35 | 0·3 | 0·3 | 0·1 | 0·13 | −0·075 | 0·083 | 0·3 | 0·005 | 0·0062 | 0·0145 |
| A.2 | 0·005 | 0·35 | 0·5 | 0·5 | 0·1 | 0·13 | −0·075 | 0·083 | 0·3 | 0·005 | 0·0084 | 0·0157 |
| A.3 | 0·005 | 0·35 | 0·5 | 0·3 | 0·1 | 0·13 | −0·075 | 0·083 | 0·3 | 0·005 | 0·0076 | 0·0149 |
| A.4 | 0·005 | 0·35 | 0·5 | 0·5 | 0·3 | 0·045 | −0·04 | 0·080 | 0·2 | 0·005 | 0·0160 | 0·0238 |
| A.5 | 0·005 | 0·35 | 1·3 | 1·3 | 0·1 | 0·125 | −0·07 | 0·081 | 0·3 | 0·005 | 0·0200 | 0·0206 |
| A.6 | 0·005 | 0·35 | 0·5 | 0·5 | 0·15 | 0·113 | −0·065 | 0·082 | 0·25 | 0·005 | 0·0103 | 0·0180 |
| B.1 | 0·005 | 0·25 | 0·5 | 0·5 | 0·1 | 0·14 | −0·065 | 0·082 | 0·3 | 0·005 | 0·0086 | 0·0159 |
| C.1 | 0·003 | 0·35 | 0·5 | 0·5 | 0·1 | 0·13 | −0·07 | 0·084 | 0·3 | 0·003 | 0·0074 | 0·0118 |
| D.1 | 0·02 | 0·35 | 0·25 | 0·25 | 0·1 | 0·125 | −0·07 | 0·081 | 0·3 | 0·02 | 0·0070 | 0·0294 |
| D.2 | 0·02 | 0·35 | 0·7 | 0·7 | 0·1 | 0·125 | −0·07 | 0·083 | 0·3 | 0·02 | 0·020 | 0·0408 |
| E.1 | 0·05 | 0·35 | 0·5 | 0·5 | 0·1 | 0·12 | −0·07 | 0·083 | 0·3 | 0·05 | 0·0204 | 0·0637 |

## TABLE 4

*Design and Shape Data for Simple Normal-Type Centre-line*

($C_{L\,\text{opt}} = 0 \cdot 2$)

| $x$ | $y_c$ | $\psi_c$ | $\varepsilon_c$ | $d\varepsilon_c/d\theta$ |
|---|---|---|---|---|
| 0 | 0 | 0 | −0·04244 | 0 |
| 0·001 | 0·0001060 | 0·003354 | −0·04229 | 0·00469 |
| 0·002 | 0·0002114 | 0·004733 | −0·04214 | 0·00662 |
| 0·003 | 0·0003167 | 0·005788 | −0·04200 | 0·00812 |
| 0·004 | 0·0004216 | 0·006676 | −0·04185 | 0·00933 |
| 0·005 | 0·0005260 | 0·007454 | −0·04170 | 0·01042 |
| 0·006 | 0·0006300 | 0·008155 | −0·04155 | 0·01139 |
| 0·0075 | 0·0007851 | 0·009099 | −0·04133 | 0·01271 |
| 0·0125 | 0·0012966 | 0·011670 | −0·04060 | 0·01627 |
| 0·02 | 0·0020464 | 0·014617 | −0·03950 | 0·02032 |
| 0·03 | 0·0030135 | 0·017666 | −0·03806 | 0·02447 |
| 0·05 | 0·0048383 | 0·022200 | −0·03523 | 0·03052 |
| 0·1 | 0·0087854 | 0·029285 | −0·02844 | 0·03947 |
| 0·2 | 0·0142603 | 0·035651 | −0·01613 | 0·04586 |
| 0·3 | 0·0169341 | 0·036953 | −0·00552 | 0·04473 |
| 0·4 | 0·0173161 | 0·035346 | +0·00342 | 0·03950 |
| 0·5 | 0·0159155 | 0·031831 | 0·01061 | 0·03185 |
| 0·6 | 0·0132417 | 0·027029 | 0·01613 | 0·02287 |
| 0·7 | 0·0098039 | 0·021394 | 0·01995 | 0·01361 |
| 0·8 | 0·0061115 | 0·015279 | 0·02207 | 0·00509 |
| 0·9 | 0·0026738 | 0·008913 | 0·02251 | −0·00127 |
| 1·0 | 0 | 0 | 0·02122 | 0 |

*Note.*—The centre-line is derived from the simple centre-line loading formula

$$g_i = \frac{C_{L\,\text{opt}}}{2\pi}(2\sin\theta + \sin 2\theta),$$

and is designed[10] to give no negative loading and a value for $C_{m0}/C_{L\,\text{opt}}$ $(= -\frac{1}{8})$ which is a minimum consistent with this. It follows, in the usual notation[9], that

$$y = \frac{C_{L\,\text{opt}}}{24\pi}(3 + \cos\theta - 3\cos 2\theta - \cos 3\theta),$$

$$\varepsilon = -\frac{C_{L\,\text{opt}}}{6\pi}(3\cos\theta + \cos 2\theta), \quad d\varepsilon_c/d\theta = \frac{C_{L\,\text{opt}}}{6\pi}(3\sin\theta + 2\sin 2\theta).$$

## TABLE 5

*Design and Shape Data for Discontinuous-Type Centre-Lines*

| Section No. | $X_1$ | $g_i(0)$ | $g_i(X_1)$ | $g_i'(X_1)$ | $g_i(1)$ | $C_{m0}$ |
|---|---|---|---|---|---|---|
| D.2/1 | 0·02 | 0·68 | 0·68 | 0·08 | 0·08 | −0·068 |
| D.2/2 | 0·02 | 0 | 0·68 | 0·08 | 0·08 | −0·075 |
| D.2/3 | 0·02 | 0·6 | 0·6 | 0 | 0 | 0·012 |
| D.2/4 | 0·02 | 0 | 0·6 | 0 | 0 | 0·006 |

*Note.*—The centre-lines were designed for use with the fairing shape D.2. The significance of the centre-line design data, $X_1$, $g_i(0)$, $g_i(X_1)$, $g_i'(X_1)$ and $g_i(1)$ is shown in Fig. 10b.

# TABLE 6

*Velocity Distributions for Symmetrical Sections*

| Section No. | Velocity Distribution $C_L = 0$ | | | Velocity Distribution $C_L = 0 \cdot 8$ | | | | Velocity Distribution $C_L = 1 \cdot 0$ | | | | Velocity Distribution $C_L = 1 \cdot 5$ | | | |
|---|---|---|---|---|---|---|---|---|---|---|---|---|---|---|---|
| | $q_1$ | $q_1'$ | $q'_{max}$ (pos.) | $q_{max}$ | $q_1$ | $q_1'$ | $q'_{max}$ | $q_{max}$ | $q_1$ | $q_1'$ | $q'_{max}$ | $q_{max}$ | $q_1$ | $q_1'$ | $q'_{max}$ |
| A.1 | 1·08 | 0·89 | | 2·86 | 2·70 | 2·22 | — | 3·36 | 3·10 | 2·55 | — | | | | |
| A.2 | 1·24 | 0·83 | 1·11 ($x$=0·35) | — | 2·95 | 1·98 | 2·04 | 3·44 | 3·37 | 2·27 | 2·31 | 4·70 | 4·43 | 2·98 | 3·02 |
| A.3 | 1·06 | 0·87 | 1·11 ($x$=0·35) | 2·91 | 2·59 | 2·11 | 2·12 | 3·41 | 2·97 | 2·42 | 2·43 | | | | |
| A.4 | 1·01 | 0·85 | 1·22 ($x$=0·05) | — | 2·41 | 2·01 | 2·07 | — | 2·76 | 2·30 | 2·34 | | | | |
| A.5 | 1·93 | 0·50 | 1·12 ($x$=0·35) | — | 3·93 | 1·02 | 1·72 | — | 4·42 | 1·15 | 1·92 | — | 5·65 | 1·47 | 2·40 |
| A.6 | 1·17 | 0·84 | 1·13 ($x$=0·15) | — | 2·78 | 1·99 | 2·05 | 3·19 | 3·18 | 2·27 | 2·32 | | | | |
| B.1 | 1·23 | 0·83 | | — | 2·93 | 1·97 | 2·03 | 3·42 | 3·35 | 2·25 | 2·31 | | | | |
| C.1 | 1·12 | 0·76 | 1·2 ($x$=0·35) | — | 3·13 | 2·10 | 2·19 | 3·63 | 3·63 | 2·44 | 2·52 | | | | |
| D.1 | 1·19 | 1·03 | 1·12 ($x$=0·35) | 2·49 | 2·09 | 1·81 | — | 2·94 | 2·32 | 2·00 | | | | | |
| D.2 | 1·64 | 0·90 | 1·12 ($x$=0·35) | — | 2·66 | 1·45 | 1·55 | — | 2·91 | 1·59 | 1·68 | 3·71 | 3·53 | 1·93 | 2·02 |
| E.1 | 1·50 | 1·01 | 1·12 ($x$=0·3) | | | | | 2·48 | 2·26 | 1·52 | 1·54 | 3·26 | 2·64 | 1·77 | 1·78 |

*Note.—See* Fig. 10c for meaning of $q_1$, $q_1'$, $q_{max}$, $q'_{max}$.

## TABLE 7a

*Velocity Distributions for Cambered Sections with Normal-Type Centre-Line*

(Camber = 1·7 per cent, $C_{L\ opt} = 0 \cdot 2$)

| Section No. | Velocity Distribution $C_L = 0 \cdot 2$ | | | Velocity Distribution $C_L = 1 \cdot 0$ | | | | Velocity Distribution $C_L = 1 \cdot 5$ | | | |
|---|---|---|---|---|---|---|---|---|---|---|---|
| | $q_1$ | $q_1'$ | $q'_{max}$ (pos.) | $q_{max}$ | $q_1$ | $q_1'$ | $q'_{max}$ | $q_{max}$ | $q_1$ | $q_1'$ | $q'_{max}$ |
| A.2/N | 1·20 | 0·81 | 1·17 ($x$=0·35) | — | 2·89 | 1·95 | 2·02 | 4·10 | 3·93 | 2·66 | 2·71 |
| A.5/N | 1·87 | 0·50 | 1·20 ($x$=0·35) | — | 3·84 | 1·02 | 1·72 | — | 5·06 | 1·34 | 2·21 |
| D.2/N | 1·63 | 0·90 | 1·20 ($x$=0·3) | — | 2·65 | 1·47 | 1·58 | 3·31 | 3·28 | 1·81 | 1·92 |
| E.1/N | 1·53 | 1·04 | 1·20 ($x$=0·3) | 2·19 | 2·16 | 1·47 | 1·50 | 2·90 | 2·54 | 1·73 | 1·74 |

## TABLE 7b

*Velocity Distributions for Cambered Sections with Discontinuous-Type Centre-Lines*

| Section No. | Velocity Distribution $C_L = 0 \cdot 2$ | | | Velocity Distribution $C_L = 1 \cdot 0$ | | | Velocity Distribution $C_L = 1 \cdot 5$ | | | Velocity Distribution $C_L = 2 \cdot 0$ | | |
|---|---|---|---|---|---|---|---|---|---|---|---|---|
| | $q_1$ | $q_1'$ | $q'_{max}$ | $q_1$ | $q_1'$ | $q'_{max}$ | $q_1$ | $q_1'$ | $q'_{max}$ | $q_1$ | $q_1'$ | $q'_{max}$ |
| D.2/1 | 2·21 | 0·61 | 1·16 | 3·45 | 0·96 | 1·43 | 4·21 | 1·17 | 1·69 | 4·96 | 1·38 | 1·95 |
| D.2/2 | 2·16 | 0·74 | 1·17 | 3·50 | 1·21 | 1·49 | 4·33 | 1·49 | 1·77 | 5·15 | 1·77 | 2·05 |
| D.2/3 | 2·67 | 0·70 | 1·16 | 3·89 | 1·02 | 1·52 | 4·64 | 1·22 | 1·76 | 5·37 | 1·41 | 2·01 |
| D.2/4 | 2·68 | 0·87 | 1·17 | 4·00 | 1·29 | 1·58 | 4·80 | 1·55 | 1·85 | 5·59 | 1·81 | 2·11 |

*Note.—See* Fig. 10c for meaning of $q_1$, $q_1'$, $q_{max}$, $q'_{max}$.)

## TABLE 8

*Velocity Distributions for Symmetrical Sections with Sink* ($C_Q$ = 0·003) *at upper surface velocity discontinuity*

| Section No. | $X_1$ | Velocity Distribution $C_L = 0 \cdot 8$ | | | Velocity Distribution $C_L = 1 \cdot 0$ | | | Velocity Distribution $C_L = 1 \cdot 5$ | | |
|---|---|---|---|---|---|---|---|---|---|---|
| | | $q_{max}$ | $q_{min}$ | $q'_{max}$ | $q_{max}$ | $q_{min}$ | $q'_{max}$ | $q_{max}$ | $q_{min}$ | $q'_{max}$ |
| A.2 | 0·005 | — | — | 1·86 | — | — | 2·10 | — | — | 2·69 |
| A.5 | 0·005 | — | — | 1·60 | — | — | 1·79 | — | — | 2·27 |
| D.2 | 0·02 | — | — | 1·50 | — | — | 1·62 | 3·78 | 3·74 | 1·92 |
| E.1 | 0·05 | | | | 2·51 | 2·41 | 1·48 | 3·29 | 2·82 | 1·71 |

## TABLE 9

*Velocity Distributions for Cambered Sections with Normal-Type Centre-Line, with Sink ($C_Q = 0 \cdot 003$) at upper surface velocity discontinuity*

(Camber $= 1 \cdot 7$ per cent, $C_{L\,opt} = 0 \cdot 2$)

| Section No. | $X_1$ | Velocity Distribution $C_L = 1 \cdot 0$ | | | Velocity Distribution $C_L = 1 \cdot 5$ | | |
|---|---|---|---|---|---|---|---|
| | | $q_{max}$ | $q_{min}$ | $q'_{max}$ | $q_{max}$ | $q_{min}$ | $q'_{max}$ |
| A.2/N | 0·005 | — | — | 1·86 | — | — | 2·46 |
| A.5/N | 0·005 | — | — | 1·62 | — | — | 2·09 |
| D.2/N | 0·02 | — | — | 1·55 | — | — | 1·85 |
| E.1/N | 0·05 | — | — | 1·47 | 2·92 | 2·68 | 1·69 |

*Note.—See* Fig. 10c for meaning of $q_{max}$, $q'_{max}$, $q_{min}$.

## TABLE 10

*Values of $C_{L\,lim}$ for Symmetrical Sections and for Cambered Versions with Normal-Type Centre-Line*

| Type of Fairing | $\varrho_L$ | $X_1$ | Symmetrical | Cambered | Symmetrical with sink | Cambered with sink |
|---|---|---|---|---|---|---|
| A.2 | 0·008 | 0·005 | 0·78 | 1·0 | 0·92 | 1·12 |
| A.5 | 0·02 | 0·005 | 1·08 | 1·28 | 1·20 | 1·48 |
| D.2 | 0·02 | 0·02 | 1·14 | 1·44 | 1·40 | 1·68 |
| E.1 | 0·02 | 0·05 | 0·72 | 0·94 | 0·86 | 1·06 |
| Lighthill section with discontinuity at a beaked leading edge. .. .. .. .. .. | | | — | 1·3 | — | 1·4 |

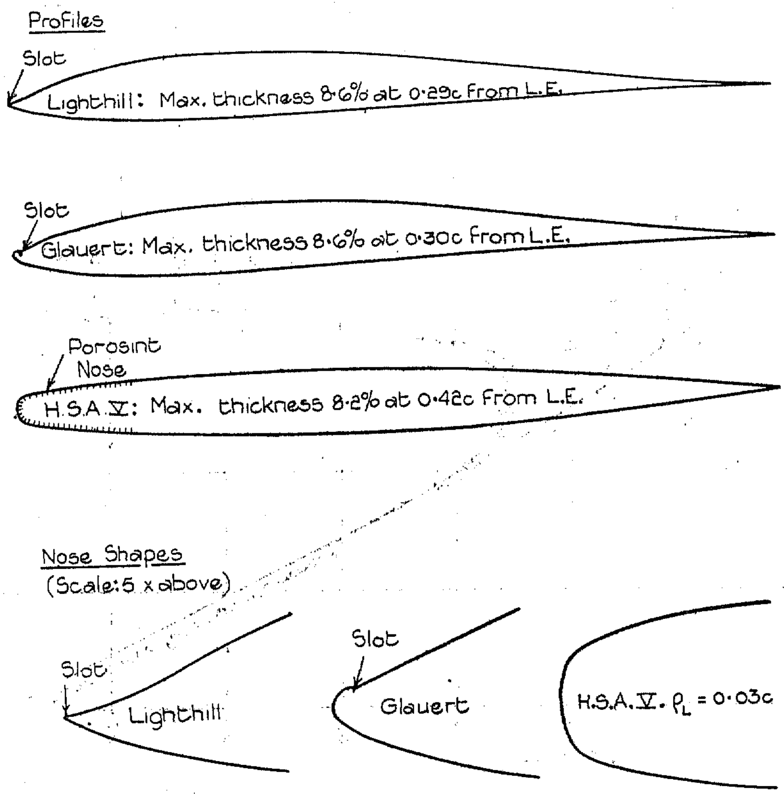


FIG. 1. Theoretical shapes of thin nose-suction aerofoils tested in N.P.L. 4-ft wind tunnel.

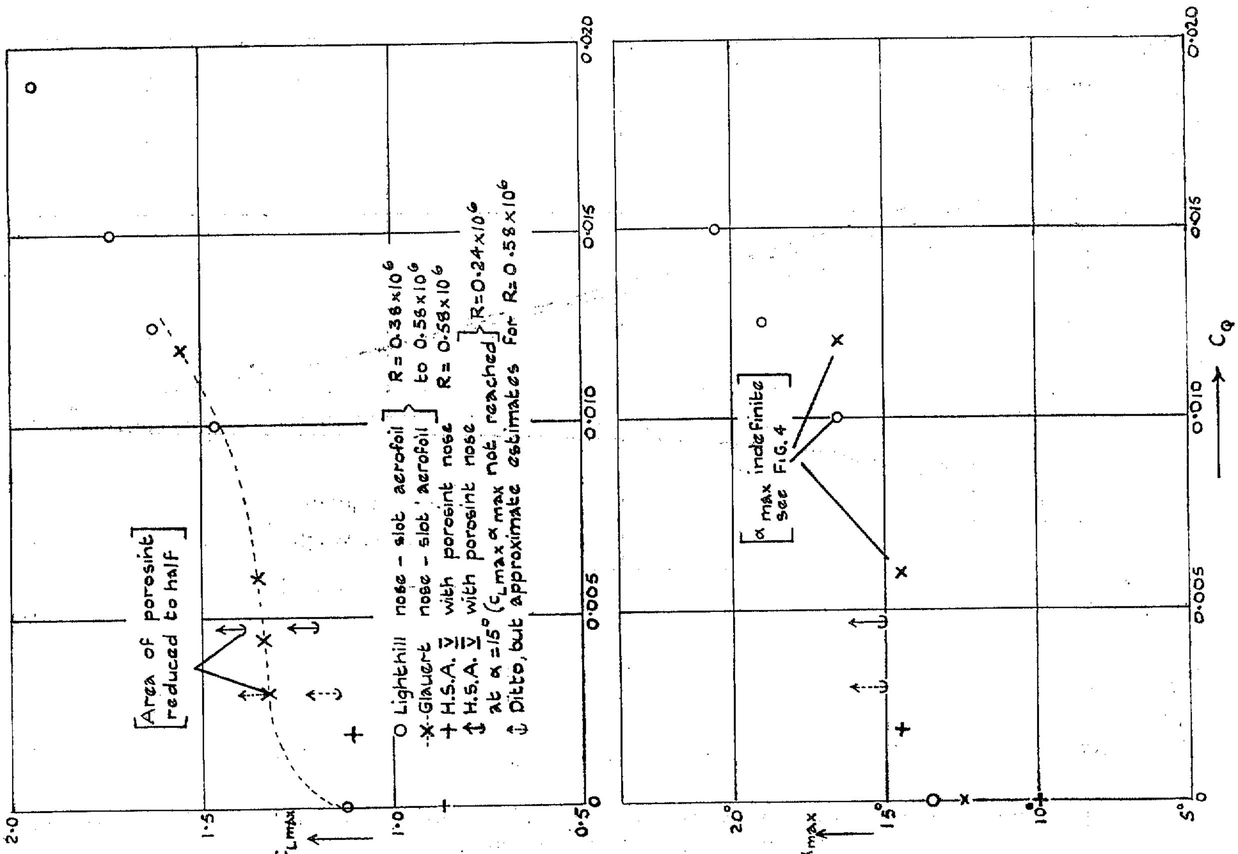


FIG. 2. Results from tests in N.P.L. 4-ft wind tunnel.

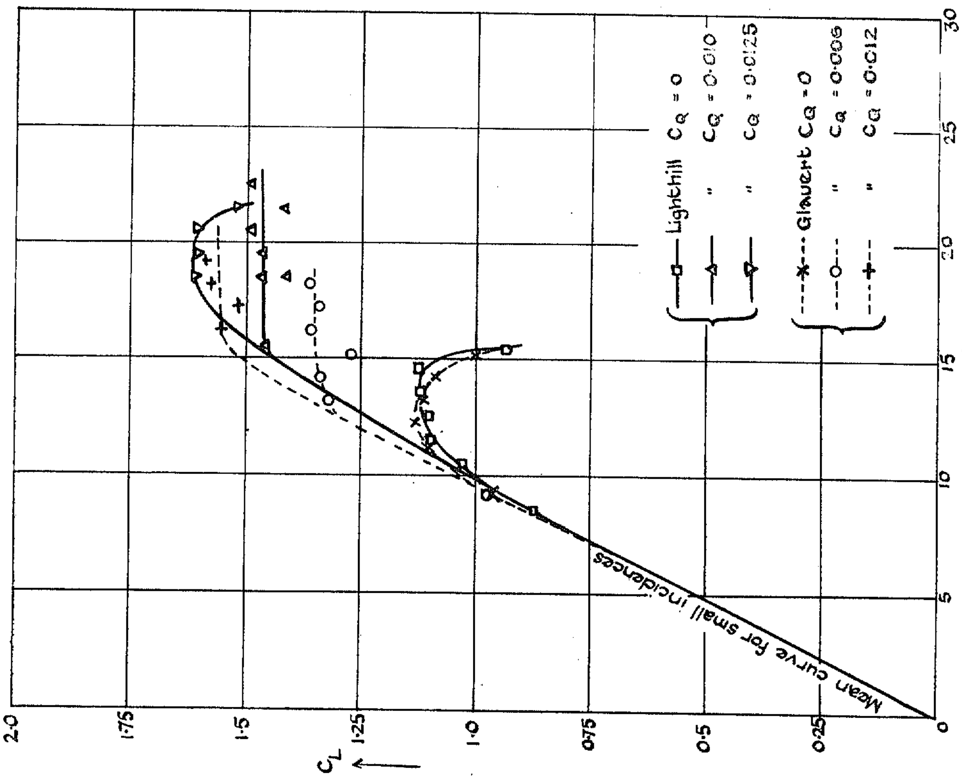


FIG. 3. Some typical experimental lift curves for Lighthill and Glauert nose-slot aerofoils ($R = 0{\cdot}38 \times 10^6$ to $0{\cdot}58 \times 10^6$).

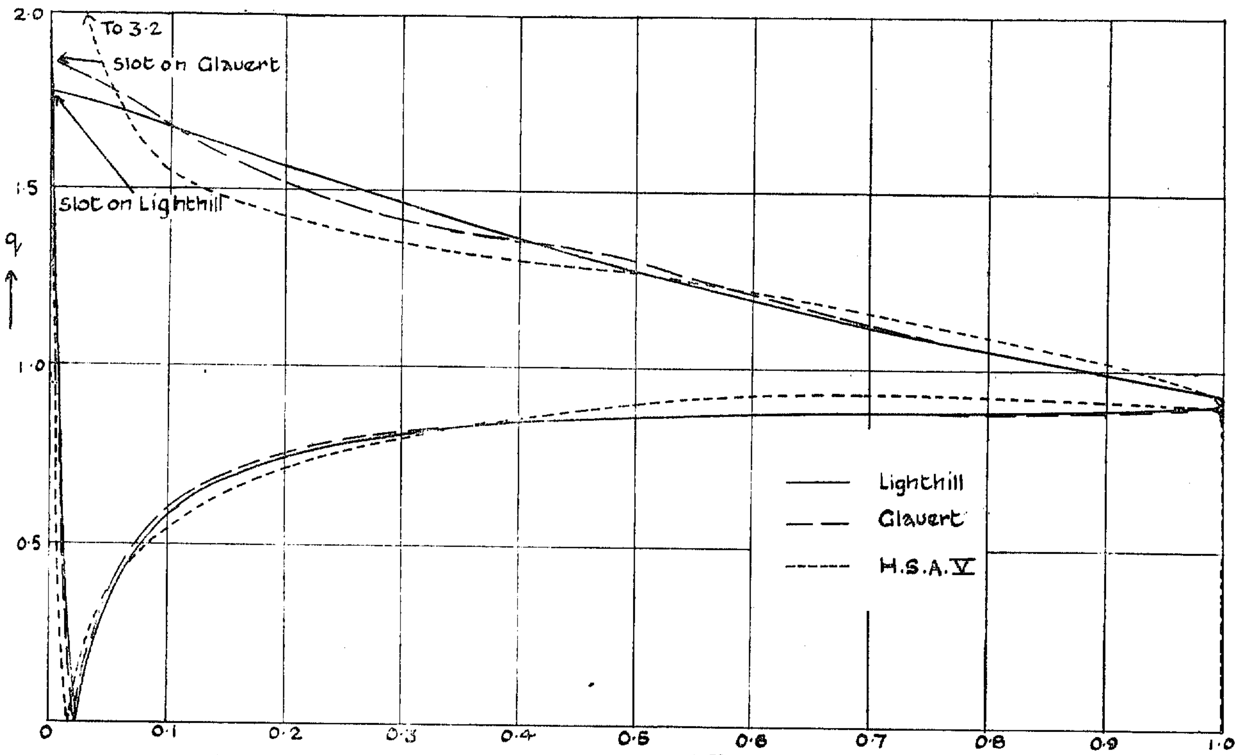


FIG. 4. Comparison of theoretical velocity distributions at 10 deg incidence for the Lighthill, Glauert and H.S.A. V aerofoils, without sink.

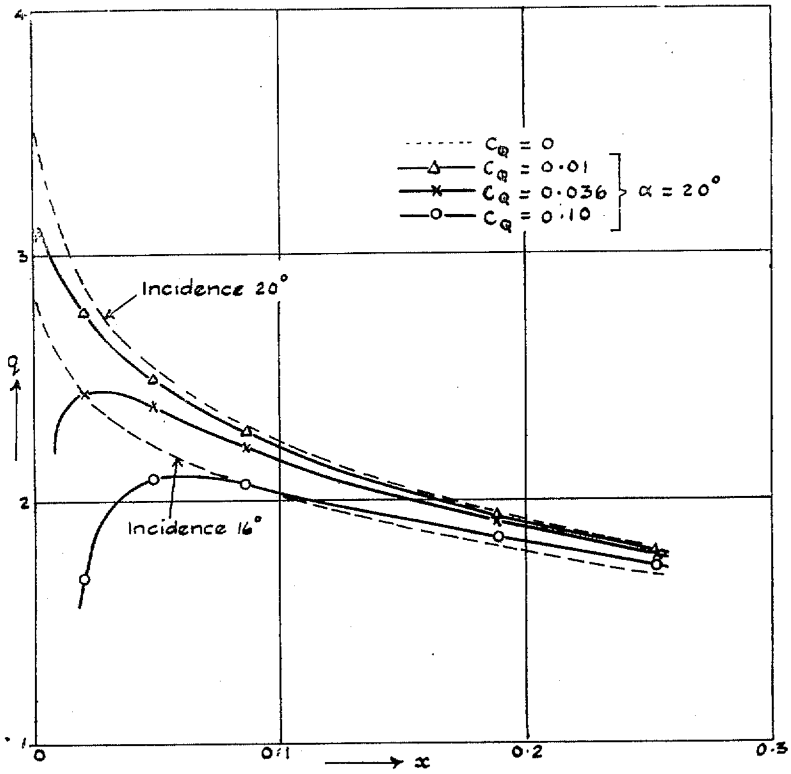


FIG. 5. Theoretical velocity distributions for Lighthill aerofoil at high incidence with sink at leading edge.

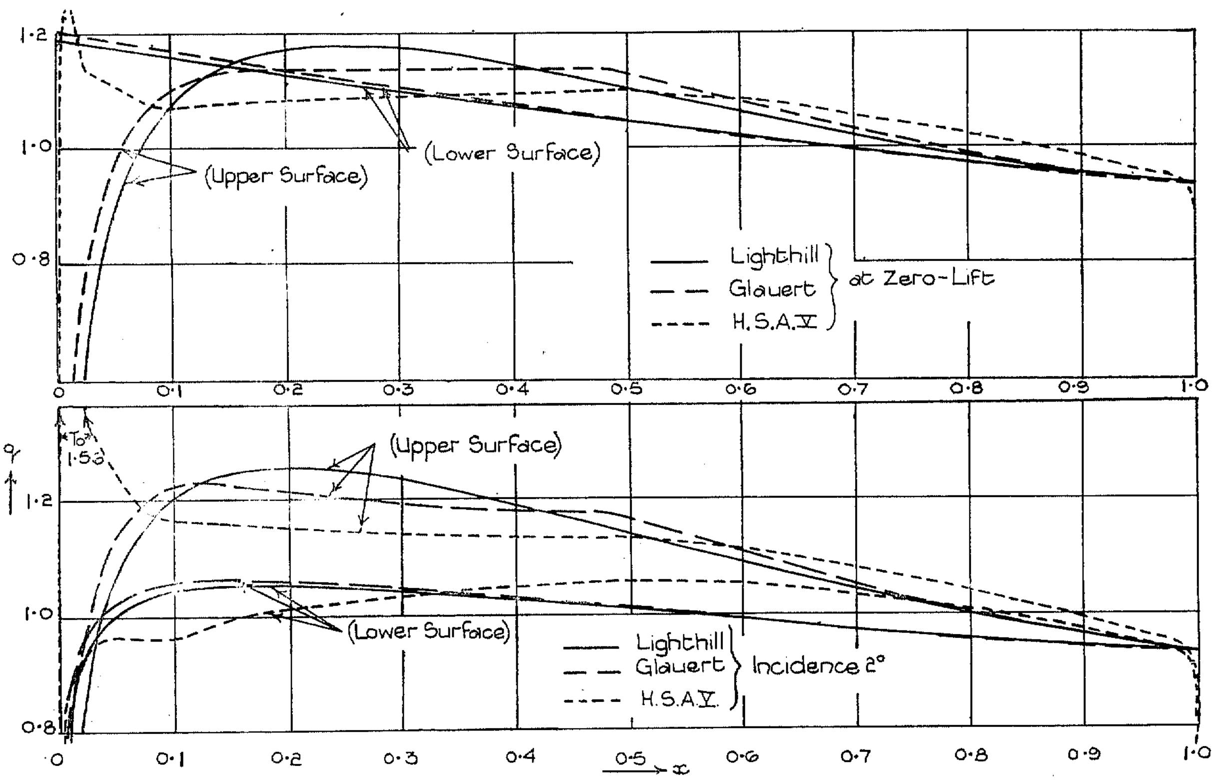


FIG. 6. Comparison of theoretical velocity distributions for the Lighthill, Glauert and H.S.A. V aerofoils at zero-lift and at 2 deg incidence, without sink.

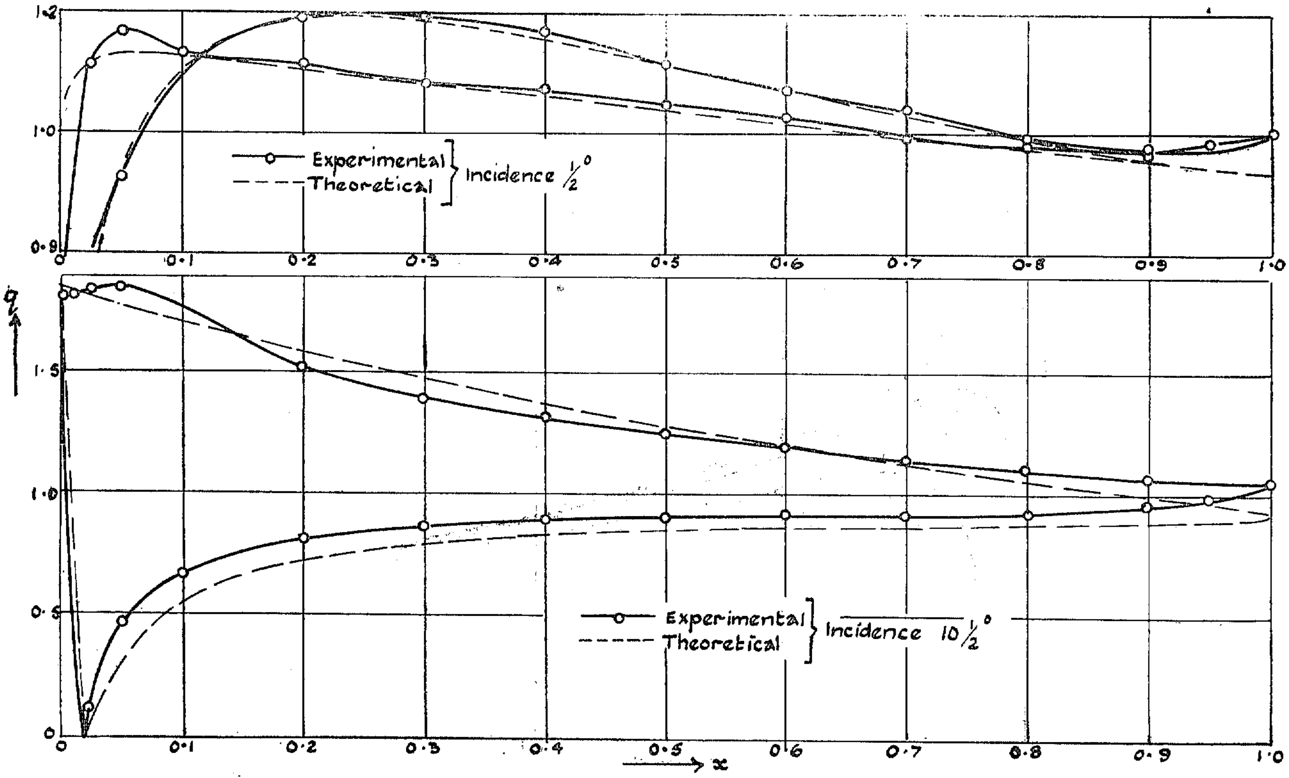


FIG. 7. Comparison of experimental and theoretical velocity distributions for Lighthill nose-slot aerofoil, without suction

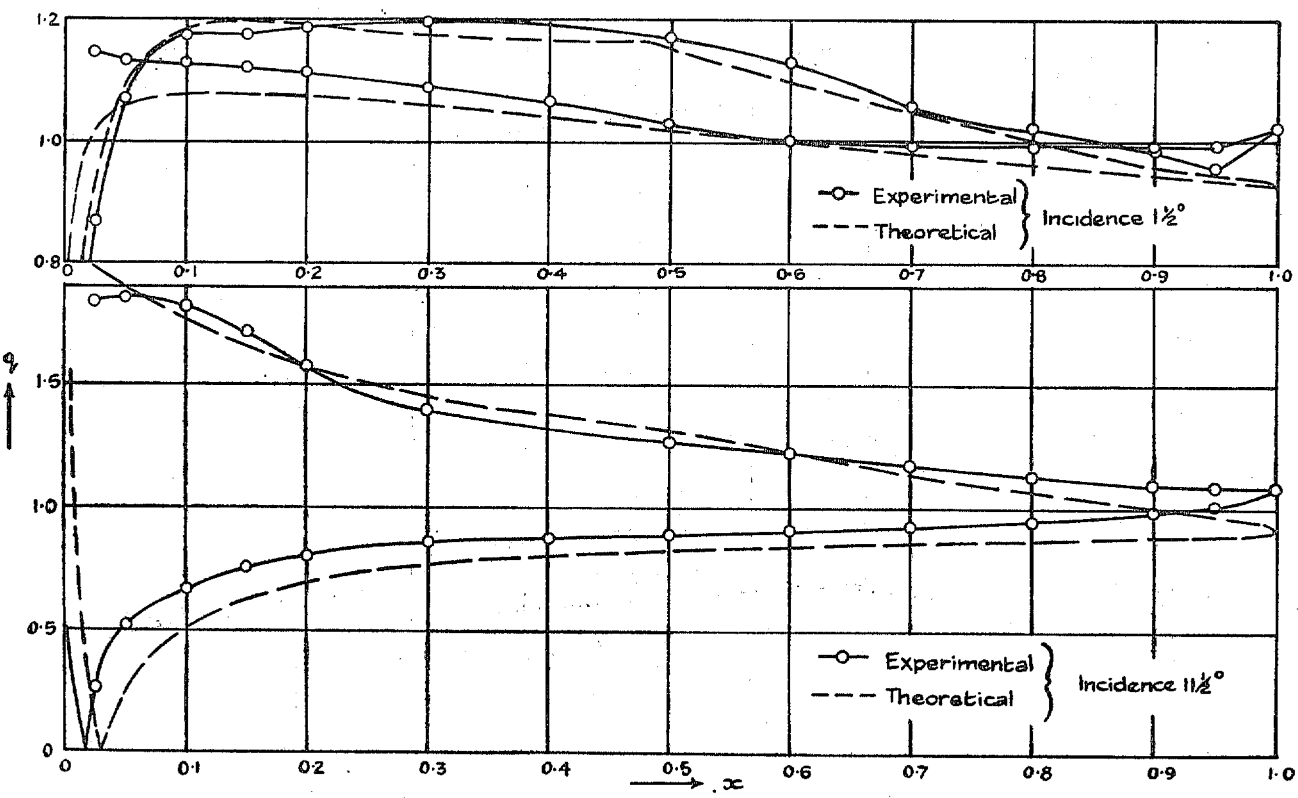


FIG. 8. Comparison of experimental and theoretical velocity distributions for Glauert nose-slot aerofoil, without suction.

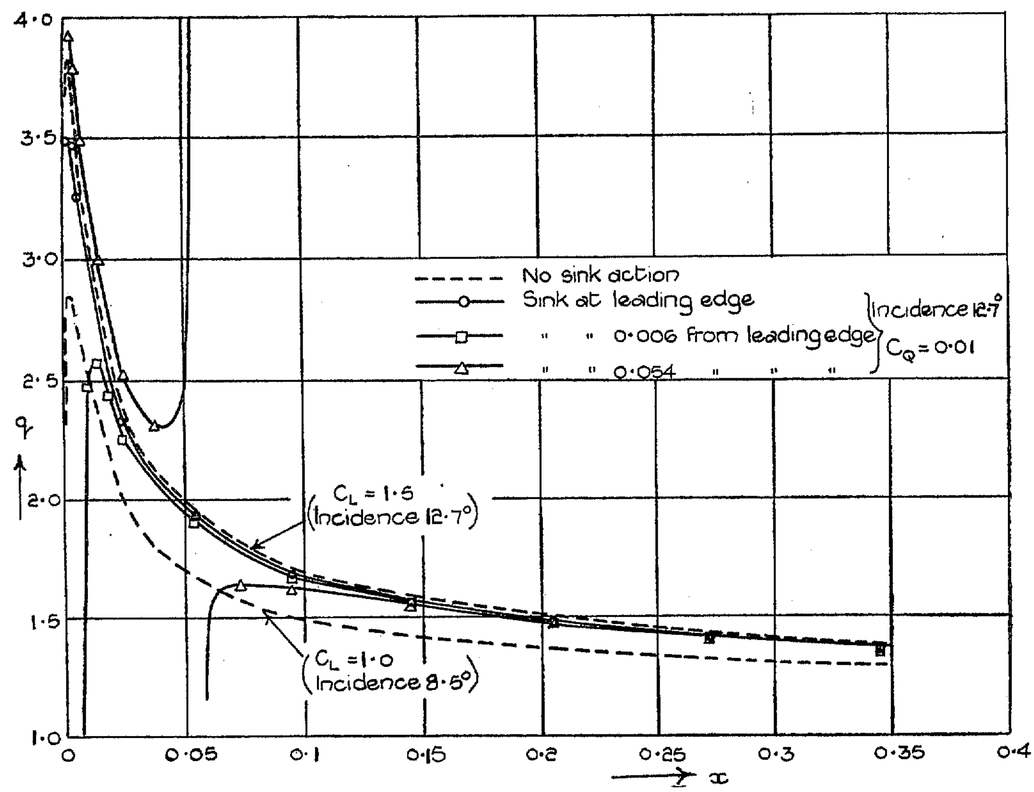


FIG. 9. Theoretical velocity distribution for H.S.A. V aerofoil at high incidences with and without sink on nose.

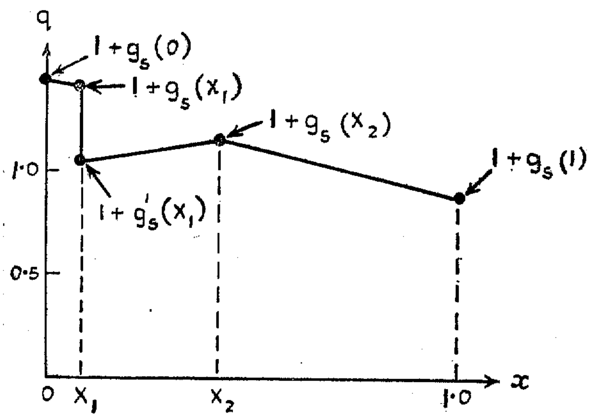


FIG. 10a. Approximation I velocity distribution $q \equiv 1 + g_s$ for symmetrical section at zero incidence.

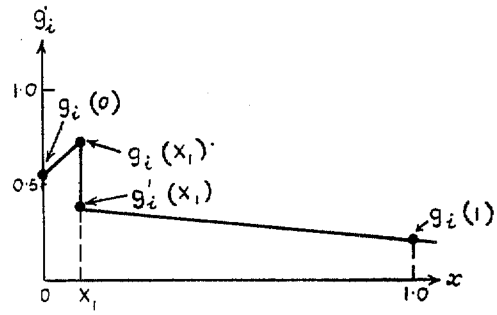


FIG. 10b. Distribution of $g_i$ for centre-line eliminating velocity discontinuity on aerofoil lower surface.

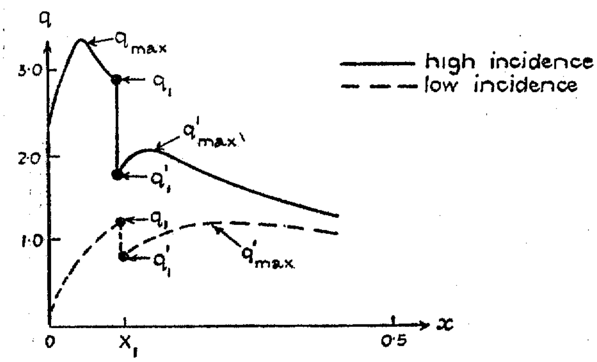


FIG. 10c. General form of Approximation III velocity distribution on upper surface.

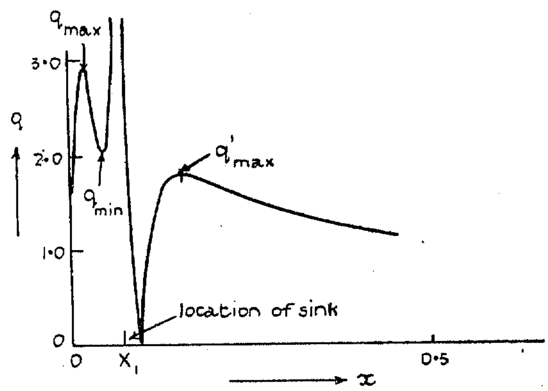


FIG. 10d. General form of Approximation III velocity distribution on upper surface, at high lift, with sink at discontinuity.

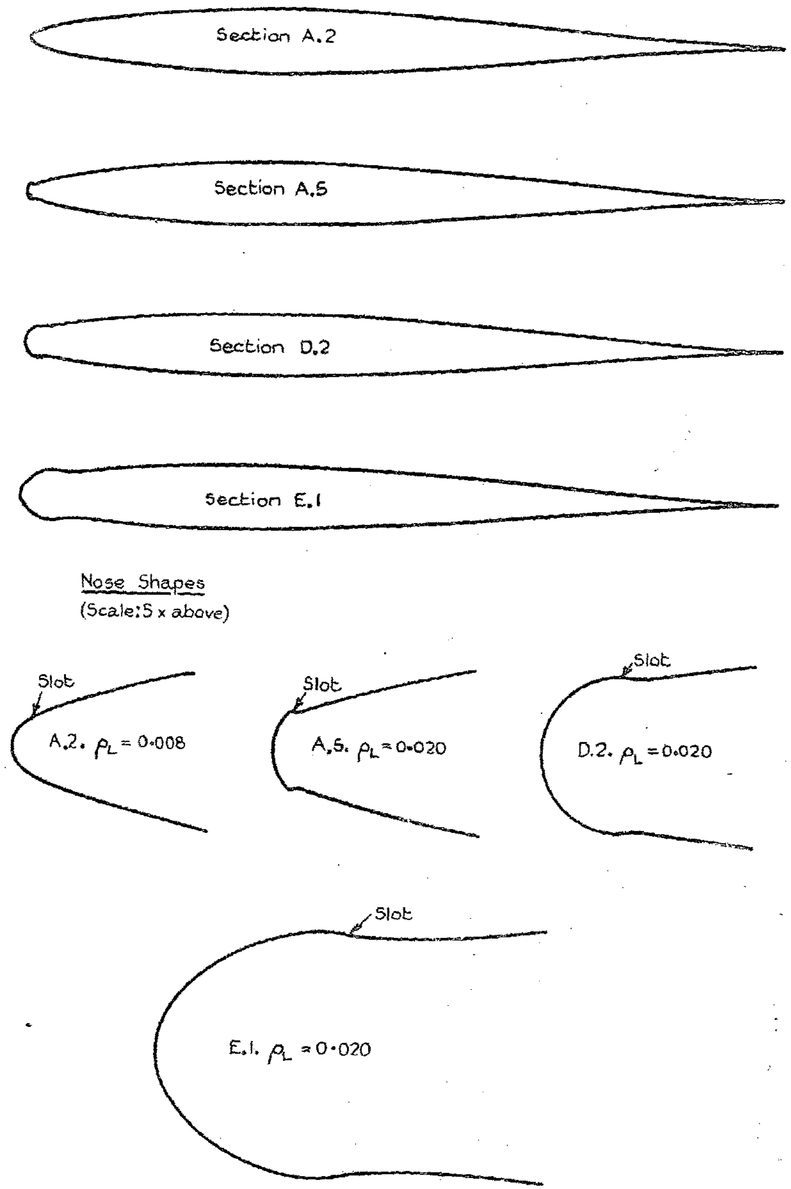


FIG. 11. Theoretical shapes of four typical symmetrical sections for nose-slot suction.

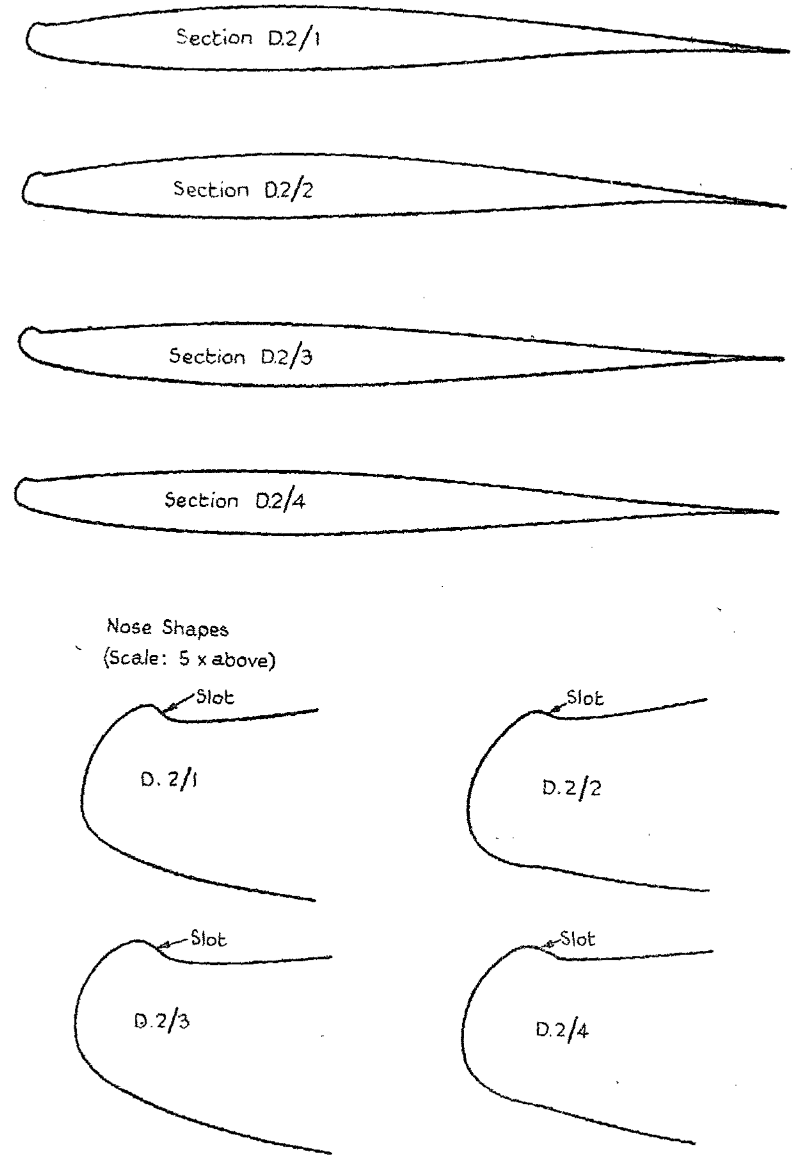


FIG. 12. Theoretical shapes of four cambered sections for nose-slot suction with fairing shape D.2 and discontinuous-type centre-lines.

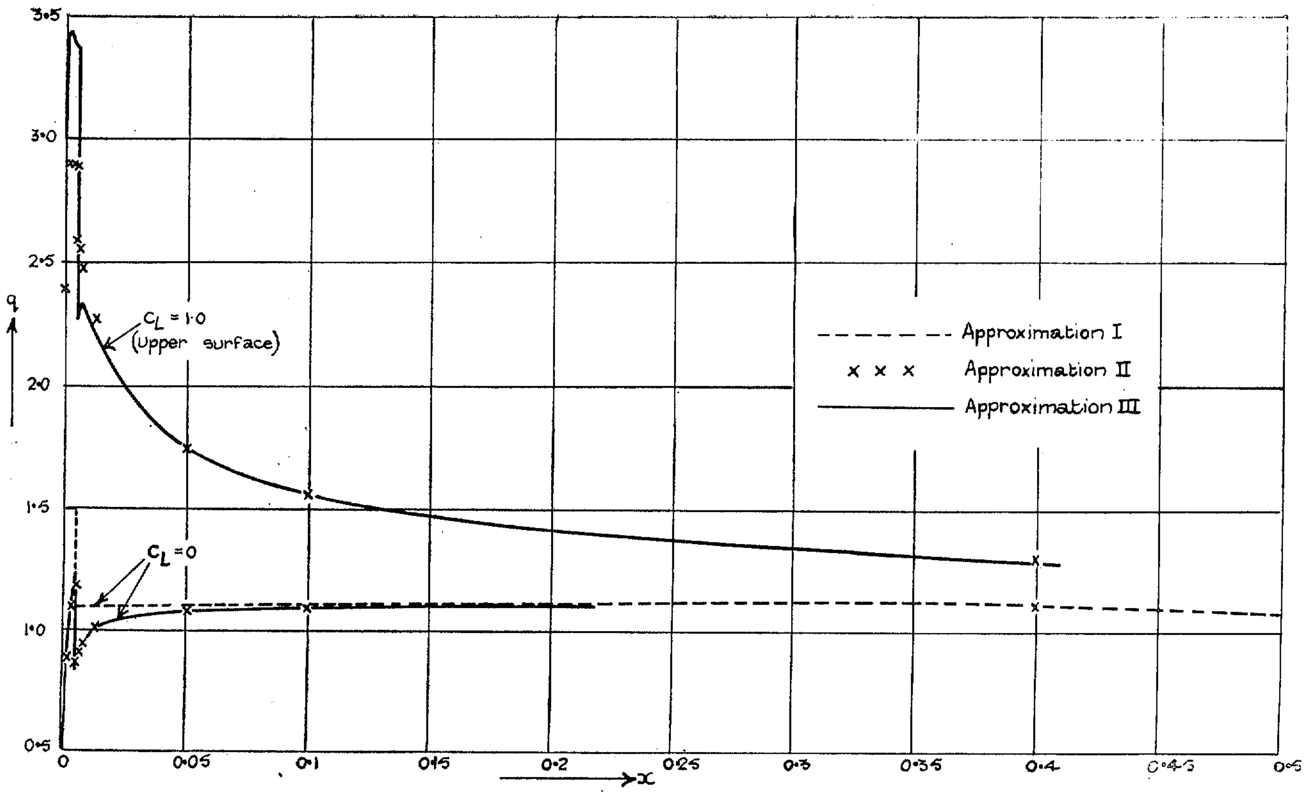


FIG. 13. Comparison of theoretical velocity distributions for symmetrical section A.2 as given by Approximations I, II and III.

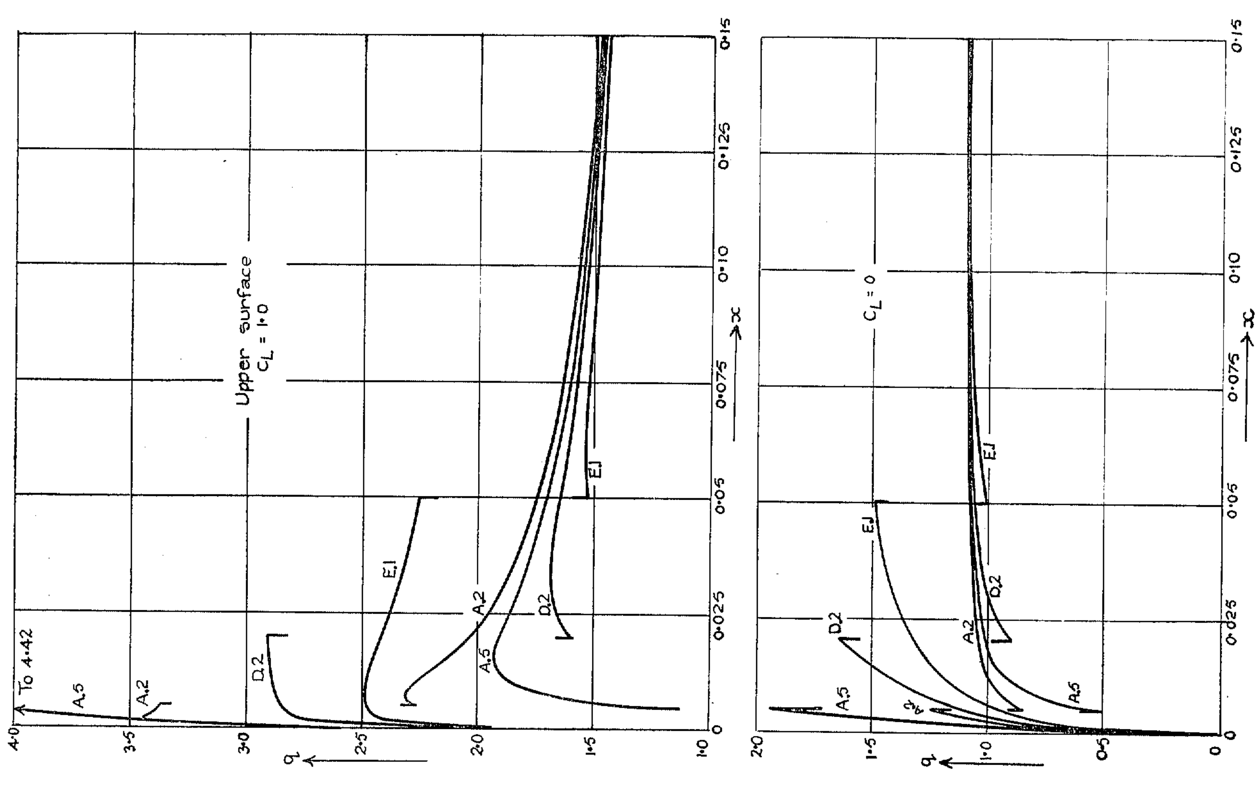


FIG. 14. Comparison of theoretical velocity distributions (without sink) for four typical symmetrical sections.

J4288 Wt.13/806 K9 3/52 D&Co. 34/263



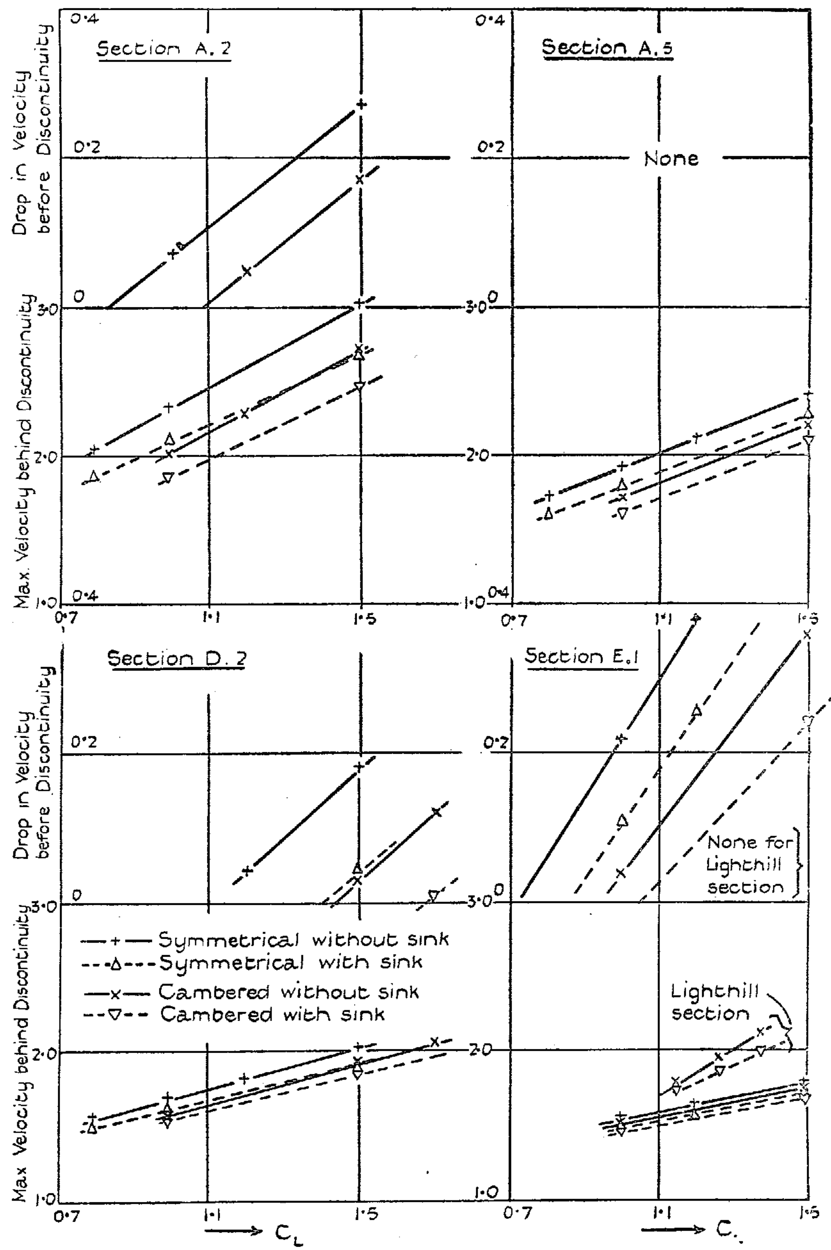


FIG. 15. Comparisons of drop in velocity before discontinuity, and of maximum velocity behind discontinuity, for symmetrical sections and for cambered versions with normal-type centre-line.

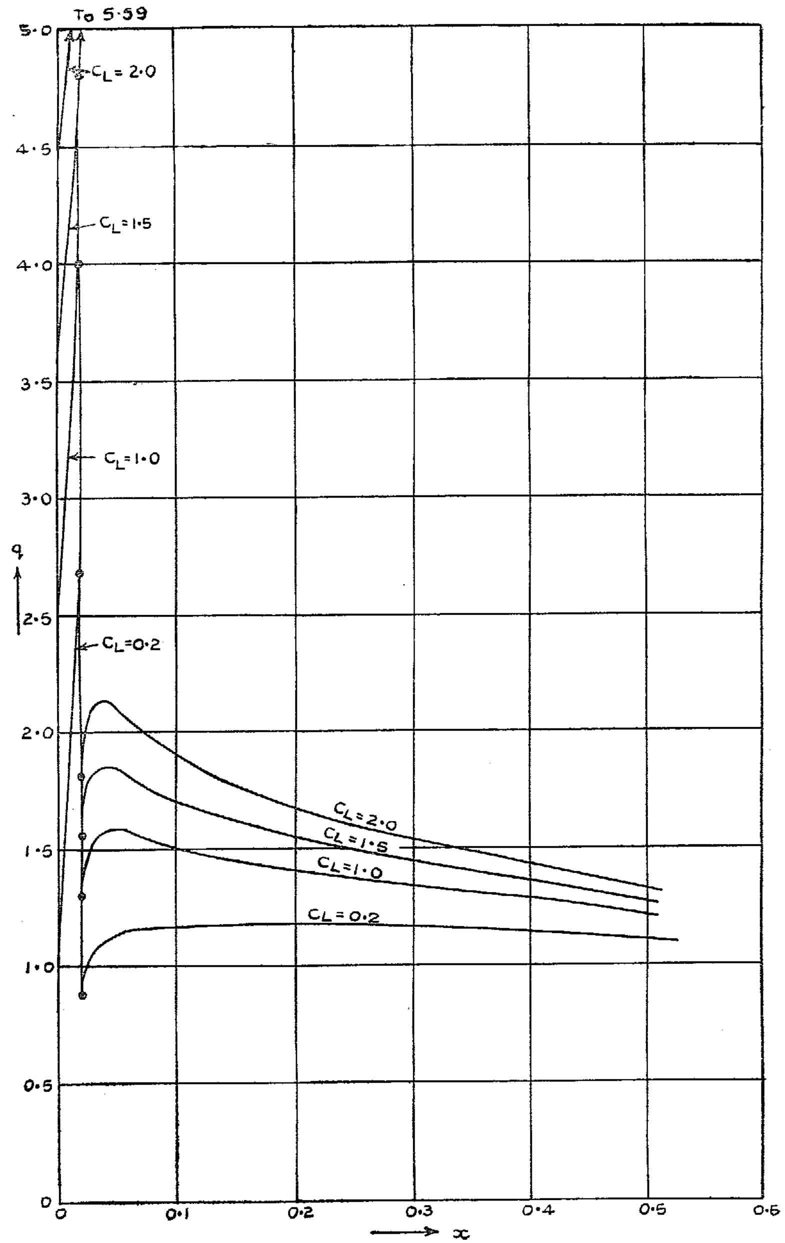


FIG. 16. Theoretical velocity distributions for cambered D.2/4 section as given by Approximation III.

PRINTED IN GREAT BRITAIN

R. & M. No. 2693
(11,560, 12,144, 13,090)
A.R.C. Technical Report

# Publications of the Aeronautical Research Council

ANNUAL TECHNICAL REPORTS OF THE AERONAUTICAL RESEARCH COUNCIL (BOUND VOLUMES)—

1934–35 Vol. I. Aerodynamics. *Out of print.*
Vol. II. Seaplanes, Structures, Engines, Materials, etc. 40*s.* (40*s.* 8*d.*)

1935–36 Vol. I. Aerodynamics. *Out of print.*
Vol. II. Structures, Flutter, Engines, Seaplanes, etc. 30*s.* (30*s.* 7*d.*)

1936 Vol. I. Aerodynamics General, Performance, Airscrews, Flutter and Spinning. 40*s.* (40*s.* 9*d.*)
Vol. II. Stability and Control, Structures, Seaplanes, Engines, etc. 50*s.* (50*s.* 10*d.*)

1937 Vol. I. Aerodynamics General, Performance, Airscrews, Flutter and Spinning. 40*s.* (40*s.* 10*d.*)
Vol. II. Stability and Control, Structures, Seaplanes, Engines, etc. 60*s.* (61*s.*)

1938 Vol. I. Aerodynamics General, Performance, Airscrews. 50*s.* (51*s.*)
Vol. II. Stability and Control, Flutter, Structures, Seaplanes, Wind Tunnels, Materials. 30*s.* (30*s.* 9*d.*)

1939 Vol. I. Aerodynamics General, Performance, Airscrews, Engines. 50*s.* (50*s.* 11*d.*)
Vol. II. Stability and Control, Flutter and Vibration, Instruments, Structures, Seaplanes, etc. 63*s.* (64*s.* 2*d.*)

1940 Aero and Hydrodynamics, Aerofoils, Airscrews, Engines, Flutter, Icing, Stability and Control, Structures, and a miscellaneous section. 50*s.* (51*s.*)

*Certain other reports proper to the 1940 volume will subsequently be included in a separate volume.*

ANNUAL REPORTS OF THE AERONAUTICAL RESEARCH COUNCIL—

| | |
|---|---|
| 1933–34 | 1*s.* 6*d.* (1*s.* 8*d.*) |
| 1934–35 | 1*s.* 6*d.* (1*s.* 8*d.*) |
| April 1, 1935 to December 31, 1936. | 4*s.* (4*s.* 4*d.*) |
| 1937 | 2*s.* (2*s.* 2*d.*) |
| 1938 | 1*s.* 6*d.* (1*s.* 8*d.*) |
| 1939–48 | 3*s.* (3*s.* 2*d.*) |

INDEX TO ALL REPORTS AND MEMORANDA PUBLISHED IN THE ANNUAL TECHNICAL REPORTS, AND SEPARATELY—

April, 1950 R. & M. No. 2600. 2*s.* 6*d.* (2*s.* 7½*d.*)

INDEXES TO THE TECHNICAL REPORTS OF THE AERONAUTICAL RESEARCH COUNCIL—

| | | |
|---|---|---|
| December 1, 1936 — June 30, 1939. | R. & M. No. 1850. | 1*s.* 3*d.* (1*s.* 4½*d.*) |
| July 1, 1939 — June 30, 1945. | R. & M. No. 1950. | 1*s.* (1*s.* 1½*d.*) |
| July 1, 1945 — June 30, 1946. | R. & M. No. 2050. | 1*s.* (1*s.* 1½*d.*) |
| July 1, 1946 — December 31, 1946. | R. & M. No. 2150. | 1*s.* 3*d.* (1*s.* 4½*d.*) |
| January 1, 1947 — June 30, 1947. | R. & M. No. 2250. | 1*s.* 3*d.* (1*s.* 4½*d.*) |

*Prices in brackets include postage.*

Obtainable from

HER MAJESTY'S STATIONERY OFFICE

York House, Kingsway, LONDON, W.C.2 423 Oxford Street, LONDON, W.1
P.O. Box 569, LONDON, S.E.1
13a Castle Street, EDINBURGH, 2 1 St. Andrew's Crescent, CARDIFF
39 King Street, MANCHESTER, 2 Tower Lane, BRISTOL, 1
2 Edmund Street, BIRMINGHAM, 3 80 Chichester Street, BELFAST

or through any bookseller.

S.O. Code No. 23-2693